



1 Characterization of Errors in Satellite-based HCHO/NO₂ 2 Tropospheric Column Ratios with Respect to Chemistry, Column to 3 PBL Translation, Spatial Representation, and Retrieval 4 Uncertainties

5
6
7 Amir H. Souri^{1*}, Matthew S. Johnson², Glenn M. Wolfe³, James H. Crawford⁴, Alan Fried⁵, Armin
8 Wisthaler^{6,7}, William H. Brune⁸, Donald R. Blake⁹, Andrew J. Weinheimer¹⁰, Tjil Verhoelst¹¹,
9 Steven Compornolle¹¹, Gaia Pinardi¹¹, Corinne Vigouroux¹¹, Bavo Langerock¹¹, Sungeon
10 Choi^{3,12}, Lok Lamsal^{3,13}, Lei Zhu^{14,15}, Shuai Sun^{14,15}, Ronald C. Cohen^{16,17}, Kyung-Eun Min¹⁸,
11 Changmin Cho¹⁸, Sajeev Philip¹⁹, Xiong Liu¹, and Kelly Chance¹

12
13 ¹Atomic and Molecular Physics (AMP) Division, Center for Astrophysics | Harvard & Smithsonian,
14 Cambridge, MA, USA

15 ²Earth Science Division, NASA Ames Research Center, Moffett Field, CA, USA

16 ³NASA Goddard Space Flight Center, Greenbelt, MD, USA

17 ⁴NASA Langley Research Center, Hampton, VA, USA

18 ⁵Institute of Arctic & Alpine Research, University of Colorado, Boulder, CO, USA

19 ⁶Institute for Ion Physics and Applied Physics, University of Innsbruck, Technikerstrasse 25, 6020
20 Innsbruck, Austria

21 ⁷Department of Chemistry, University of Oslo, P.O. box 1033, Blindern, 0315 Oslo, Norway

22 ⁸Department of Meteorology and Atmospheric Science, Pennsylvania State University, University Park,
23 PA, USA

24 ⁹Department of Chemistry, University of California, Irvine, CA, USA

25 ¹⁰National Center for Atmospheric Research, Boulder, CO, USA

26 ¹¹Royal Belgian Institute for Space Aeronomy (BIRA-IASB), Ringlaan 3, 1180 Uccle, Belgium

27 ¹²Science Systems and Applications, Inc., Lanham, MD 20706, USA

28 ¹³Universities Space Research Association, Columbia, MD 21046, USA

29 ¹⁴School of Environmental Science and Engineering, Southern University of Science and Technology,
30 Shenzhen, Guangdong, China

31 ¹⁵Guangdong Provincial Observation and Research Station for Coastal Atmosphere and Climate of the
32 Greater Bay Area, Shenzhen, Guangdong, China

33 ¹⁶Department of Earth and Planetary Science, University of California Berkeley, Berkeley, CA 94720, USA

34 ¹⁷Department of Chemistry, University of California Berkeley, Berkeley, CA 94720, USA

35 ¹⁸School of Earth Sciences and Environmental Engineering, Gwangju Institute of Science and Technology,
36 Gwangju, South Korea

37 ¹⁹Centre for Atmospheric Sciences, Indian Institute of Technology Delhi, New Delhi, India

38
39 * Corresponding Author: ahsouri@cfa.harvard.edu
40

41 **Abstract.**

42 The availability of formaldehyde (HCHO) (a proxy for volatile organic compound
43 reactivity) and nitrogen dioxide (NO₂) (a proxy for nitrogen oxides) tropospheric columns from
44 Ultraviolet-Visible (UV-Vis) satellites has motivated many to use their ratios to gain some insights
45 into the near-surface ozone sensitivity. Strong emphasis has been placed on the challenges that
46 come with transforming what is being observed in the tropospheric column to what is actually in
47 the planetary boundary layer (PBL) and near to the surface; however, little attention has been paid



48 to other sources of error such as chemistry, spatial representation, and retrieval uncertainties. Here
49 we leverage a wide spectrum of tools and data to carefully quantify those errors.

50 Concerning the chemistry error, a well-characterized box model constrained by more than
51 500 hours of aircraft data from NASA's air quality campaigns is used to simulate the ratio of the
52 chemical loss of HO₂+RO₂ (LRO_x) to the chemical loss of NO_x (LNO_x). Subsequently, we
53 challenge the predictive power of HCHO/NO₂ ratios (FNRs), which are commonly applied in
54 current research, at detecting the underlying ozone regimes by comparing them to LRO_x/LNO_x.
55 FNRs show a strongly linear ($R^2=0.94$) relationship to LRO_x/LNO_x in the log-log scale. Following
56 the baseline (i.e., $\ln(\text{LRO}_x/\text{LNO}_x) = -1.0 \pm 0.2$) with the model and mechanism (CB06, r2) used for
57 segregating NO_x-sensitive from VOC-sensitive regimes, we observe a broad range of FNR
58 thresholds ranging from 1 to 4. The transitioning ratios strictly follow a Gaussian distribution with
59 a mean and standard deviation of 1.8 and 0.4, respectively. This implies that FNR has an inherent
60 20% standard error (1-sigma) resulting from not being able to fully describe the RO_x-HO_x cycle.
61 We calculate high ozone production rates (PO₃) dominated by large HCHO×NO₂ concentration
62 levels, a new proxy for the abundance of ozone precursors. The relationship between PO₃ and
63 HCHO×NO₂ becomes more pronounced when moving towards NO_x-sensitive regions due to non-
64 linear chemistry; our results indicate that there is fruitful information in the HCHO×NO₂ metric
65 that has not been utilized in ozone studies. The vast amount of vertical information on HCHO and
66 NO₂ concentration from the air quality campaigns enables us to parameterize the vertical shapes
67 of FNRs using a second-order rational function permitting an analytical solution for an altitude
68 adjustment factor to partition the tropospheric columns to the PBL region. We propose a
69 mathematical solution to the spatial representation error based on modeling isotropic
70 semivariograms. With respect to a high-resolution sensor like TROPospheric Monitoring
71 Instrument (TROPOMI) (>5.5×3.5 km²), Ozone Monitoring Instrument (OMI) loses 12% of
72 spatial information at its native resolution. A pixel with a grid size of 216 km² fails at capturing
73 ~65% of the spatial information in FNRs at a 50 km length scale comparable to the size of a large
74 urban center (e.g., Los Angeles). We ultimately leverage a large suite of in-situ and ground-based
75 remote sensing measurements to draw the error distributions of daily TROPOMI and OMI
76 tropospheric NO₂ and HCHO columns. At 68% confidence interval (1 sigma) errors pertaining to
77 daily TROPOMI observations, either HCHO or tropospheric NO₂ columns should be above 1.2-
78 1.5×10¹⁶ molec.cm⁻² to attain 20-30% standard error in the ratio. This level of error is almost non-
79 achievable with OMI given its large error in HCHO.

80 The satellite column retrieval error is the largest contributor to the total error (40-90%) in
81 the FNRs. Due to a stronger signal in cities, the total relative error (<50%) tends to be mild,
82 whereas areas with low vegetation and anthropogenic sources (e.g., Rocky Mountains) are
83 markedly uncertain (>100%). Our study suggests that continuing development in the retrieval
84 algorithm and sensor design and calibration is essential to be able to advance the application of
85 FNRs beyond a qualitative metric.

86 1. Introduction

87 Accurately representing the near-surface ozone (O₃) sensitivity to its two major precursors,
88 nitrogen dioxides (NO_x) and volatile organic compounds (VOCs), is an imperative step in
89 understanding non-linear chemistry associated with ozone production rates in the atmosphere.
90 While it is often tempting to characterize an airshed as NO_x or VOC-sensitive, both conditions are
91 expected as VOC-sensitive conditions near NO_x sources transition to NO_x-sensitive conditions
92 downwind as NO_x dilutes. Thus, reducing the footprint of ozone production can mostly be
93 achieved through NO_x reductions. VOCs are key to determining both the location and peak in



94 ozone production which varies nonlinearly to the NO_x abundance. Thus, knowledge of the relative
95 levels of NO_x and VOCs informs the trajectory of ozone production and expectations of where
96 peak ozone will occur as emissions change. While the near-surface ambient nitrogen dioxide (NO₂)
97 concentrations are regularly monitored by a large number of surface stations, the measurements of
98 several VOCs with different reactivity rates with respect to hydroxyl (OH), are not routinely
99 available. As such, our knowledge on where and when ozone production rates are elevated, and
100 their quantitative dependence on a long list of ozone precursors, is fairly limited, except for
101 observationally-rich air quality campaigns. This limitation has prompted several studies such as
102 Sillman et al. (1990), Tonnesen and Dennis (2000a,b), and Sillman and He (2002) to investigate if
103 the ratio of certain measurable compounds can diagnose ozone regimes meaning if the ozone
104 production rate is sensitive to NO_x (i.e., NO_x-sensitive) or VOC (i.e., VOC-sensitive). Sillman
105 and He (2002) suggested that H₂O₂/HNO₃ was a robust measurable ozone indicator as this ratio
106 could well describe the chemical loss of HO₂+RO₂ (LRO_x) to the chemical loss of NO_x (LNO_x)
107 controlling the O₃-NO_x-VOC chemistry (Kleinman et al., 2001). Nonetheless, both H₂O₂ and
108 HNO₃ measurements are limited to few spatially-sparse air quality campaigns.

109 Formaldehyde (HCHO) is an oxidation product of VOCs and its relatively short lifetime
110 (~1-9 hr) makes the location of its primary and secondary sources rather identifiable (Seinfeld and
111 Pandis, 2006; Fried et al., 2020). Fortunately, monitoring HCHO abundance in the atmosphere has
112 been a key goal of many Ultraviolet-Visible (UV-Vis) viewing satellites for decades (Chance et
113 al., 1991; Chance et al., 1997; Chance et al., 2000; González Abad et al., 2015; De Smedt et al.,
114 2008, 2012, 2015, 2018, 2021) with reasonable spatial coverage. Additionally, the strong
115 absorption of NO₂ in the UV-Vis range has permit measurements of NO₂ columns from space
116 (Martin et al., 2002; Boersma et al., 2004, 2007, 2018).

117 Advancements in satellite remote-sensing of these two key compounds have encouraged
118 many studies to elucidate if the ratio of HCHO/NO₂ (hereafter FNR) could be a robust ozone
119 indicator (Tonnesen and Dennis, 2000b; Martin et al. 2004, Duncan et al., 2010). Most studies
120 using the satellite-based FNR columns attempted to provide a qualitative view of the underlying
121 chemical regimes (e.g., Choi et al., 2012; Choi and Souri, 2015a,b; Jin and Holloway, 2015; Souri
122 et al., 2017; Jeon et al., 2018; Lee et al., 2021). Relatively few studies (Duncan et al., 2010; Jin et
123 al., 2017; Schroeder et al., 2017; Souri et al., 2020) have carefully tried to provide a quantitative
124 view of the usefulness of the ratio. For the most part, the inhomogeneous vertical distribution of
125 FNR in columns has been emphasized. Jin et al. (2017) and Schroeder et al. (2017) showed that
126 differing vertical shapes of HCHO and NO₂ can cause the vertical shape of FNR not to be
127 consistent throughout the troposphere leading to a variable relationship between what is being
128 observed from the satellite and what is actually occurring in the lower atmosphere. Jin et al. (2017)
129 calculated an adjustment factor to translate the column to the surface using a relatively coarse
130 global chemical transport model. The adjustment factor showed a clear seasonal cycle stemming
131 from spatial and temporal variability associated with the vertical sources and sinks of HCHO and
132 NO₂, in addition to the atmospheric dynamics. In a more data driven approach, Schroeder et al.
133 (2017) found that the detailed differences in the boundary layer vertical distributions of HCHO
134 and NO₂ lead to a wide range of ambiguous ratios. Additionally, ratios were shown to shift on high
135 ozone days, raising questions regarding the value of satellite averages over longer timescales. A
136 goal for our research is to put together an integrated and data-driven mathematical formula to
137 translate the tropospheric column to the PBL, exploiting the abundant aircraft measurements
138 available during ozone seasons.



139 Using observationally-constrained box models, Souri et al. (2020) demonstrated that there
140 was a fundamentally inherent uncertainty related to the ratio originating from the chemical
141 dependency of HCHO on NO_x (Wolfe et al., 2016). In VOC-rich (poor) environments, the
142 transitioning ratios from NO_x-sensitive to VOC-sensitive occurred in larger (smaller) values than
143 the conventional thresholds defined in Duncan et al. (2010) due to an increased (dampened) HCHO
144 production induced by NO_x. To account for the chemical feedback and to prevent a wide range of
145 thresholds on segregating NO_x-sensitive from VOC-sensitive regions, Souri et al. (2020)
146 suggested using a first-order polynomial matched to the ridgeline in P(O₃) isopleths. Their study
147 illuminated the fact that the ratio suffers from an inherent chemical complication. However, Souri
148 et al. (2020) did not quantify the error and their work was limited to a subset of atmospheric
149 condition. To challenge the predictive power of FNR from chemistry perspective, we will take
150 advantage of a large suite of datasets to make maximum use of varying meteorological and
151 chemical conditions.

152 Not only are satellite-based column measurements unable to resolve the vertical
153 information of chemical species in the tropospheric column, but they are also unable to resolve the
154 horizontal spatial variability due to their spatial footprint. The larger the footprint is, the more
155 horizontal information is blurred out. For instance, Souri et al. (2020) observed a substantial spatial
156 variance (information) in FNR columns at the spatial resolution of 250×250 m² observed by an
157 airborne sensor over Seoul, South Korea. It is intuitively clear that a coarse resolution sensor would
158 lose a large degree of spatial variance (information). This error, known as the spatial representation
159 error, has not been studied with respect to FNR. We will leverage what we have learned from Souri
160 et al. (2022), which modeled the spatial heterogeneity in discrete data using geostatistics, to
161 quantify the spatial representation error in the ratio over an urban environment.

162 A longstanding challenge is to have a reliable estimate on the satellite retrieval errors of
163 tropospheric column NO₂ and HCHO. Significant efforts have been made recently to assemble,
164 analyze, and estimate the retrieval errors for two key satellite sensors, TROPOspheric Monitoring
165 Instrument (TROPOMI) and Ozone Monitoring Instrument (OMI), using various in-situ
166 measurements (Verhoelst et al., 2021; Vigouroux et al., 2020; Choi et al., 2020; Laughner et al.,
167 2019; Zhu et al., 2020). In this study, we will exploit paired comparisons from some of these new
168 studies to propagate individual uncertainties in HCHO and NO₂ to the FNR errors.

169 The overarching science goal of this study is to address the fact that the accurate diagnosis
170 of surface O₃ photochemical regimes is impeded by numerous uncertainty components, which will
171 be addressed in the current paper, and can be classified into four major categories: i) inherent
172 uncertainties associated with the approach of FNRs to diagnose local O₃ production and sensitivity
173 regimes, ii) translation of tropospheric column satellite retrievals to represent PBL- or surface-
174 level chemistry, iii) spatial representativity of ground pixels of satellite sensors, and iv)
175 uncertainties associated with satellite-retrieved column-integrated concentrations of HCHO and
176 NO₂. We will address all of these sources of uncertainty using a broad spectrum of data and tools.

177 Our paper is organized with the following sections. Section 2 describes the chemical box
178 model setup and data applied. Sections 3.1 to 3.4 deal with chemistry aspects of FNRs and show
179 the results from the box model. Section 3.5 introduces a data-driven framework to transform the
180 FNR tropospheric columns to the PBL region. Section 3.6 offers a new way to quantify the spatial
181 representation error in satellites. Section 3.7 deals with the satellite error characterization and their
182 impacts on the ratio. Section 3.8 summarizes the fractional contribution of each error to the total
183 error. Finally, Sect. 4 provides a summary and conclusions of the study.



184 2. Photochemical Box Modeling and Aircraft Data Used

185 To quantify the uncertainty of FNR from a chemical perspective, and to obtain several
186 imperative parameters including the calculated ozone production rates, and the loss of NO_x (LNO_x)
187 and RO_x (LRO_x), we utilize the Framework for 0-D Atmospheric Modeling (F0AM) v4 (Wolfe et
188 al., 2016). We adopt the Carbon Bond 6 (CB06, r2) chemical mechanism and heterogenous
189 chemistry is not considered in our simulations. The model is initialized with the measurements of
190 several compounds, many of which constrain the model by being held constant for each timestep
191 (see Table 1). It is important to acknowledge that the VOC constraints for these model calculations
192 are incomplete, especially for the DISCOVER-AQ campaigns which lacked comprehensive VOC
193 observations. Nevertheless, we will show that the selected VOCs are sufficient to reproduce a large
194 variance (>70%) in observed HCHO.

195 Figure 1 shows the map of data points from Deriving Information on Surface Conditions
196 from Column and Vertically Resolved Observations Relevant to Air Quality (DISCOVER-AQ)
197 Baltimore-Washington (2011), DISCOVER-AQ Houston-Texas (2013), DISCOVER-AQ
198 Colorado (2014), and Korea United States Air Quality Study (KORUS-AQ) (2016).
199 Meteorological inputs come from the observed pressure, temperature, and relative humidity. The
200 measurements of photolysis rates are not available for all photolysis reactions; therefore, our initial
201 guess of those rates comes from a look-up-table populated by the National Center for Atmospheric
202 Research (NCAR) Tropospheric Ultraviolet And Visible (TUV) model calculations. These values
203 are a function of solar zenith angle, total ozone column density, surface albedo, and altitude. We
204 set the total ozone column and the surface albedo to fixed numbers of 325 (Dobson) DU and 0.15,
205 respectively. The initial guess is then corrected by applying the ratio of observed photolysis rates
206 of $\text{NO}_2+h\nu$ ($j\text{NO}_2$) and/or $\text{O}_3+h\nu$ ($j\text{O}^1\text{D}$) to the calculated ones to all j -values (i.e., wavelength
207 independent). If both observations of $j\text{NO}_2$ and $j\text{O}^1\text{D}$ are available, the correction factor is
208 averaged. The KORUS-AQ campaign is the only one that provides $j\text{O}^1\text{D}$ measurements; therefore
209 the use of the wavelength-independent correction factor based on the observed to calculated $j\text{NO}_2$
210 values for all j -values including $j\text{O}^1\text{D}$ is a potential source of error in the model especially when
211 aerosols are present. The model calculations are based on the observations merged to a temporal
212 resolution varying from 10 to 15 seconds. Each calculation was run for five consecutive days with
213 an integration time of 1 hour to approach diel steady state. Some secondarily-formed species must
214 be unconstrained for the purpose of model validation. Therefore, the concentrations of several
215 secondarily-formed compounds such as HCHO and PAN are unconstrained. Nitric oxide (NO) and
216 NO_2 are also allowed to cycle, while their sum (i.e., NO_x) is constrained. Because the model does
217 not consider various physical loss pathways including deposition and transport, we oversimplify
218 their physical loss through a first-order dilution rate set to $1/86400-1/43200 \text{ s}^{-1}$ (i.e., 24- or 12-hr
219 lifetime), which in turn prevents relatively long-lived species from accumulating over time. The
220 optimal dilution rate is determined to ensure a marginal difference between the average of
221 simulated HCHO and observations (<5%) for each air quality campaign. The dilution factor is set
222 to a fixed value for an entire campaign. Each time tag is independently simulated meaning we do
223 not initialize the next run using the simulated values from the previous one; this in turn permits
224 parallel computation. Table 1 lists the major configuration along with the observations used for
225 the box model.

226 Several parameters are calculated based on the box model outputs. LRO_x is defined through
227 the sum of primarily radical-radical reactions:



$$LRO_x = k_{HO_2+HO_2}[HO_2]^2 + \sum k_{RO_{2i}+HO_2}[RO_{2i}][HO_2] + \sum k_{RO_{2i}+RO_{2i}}[RO_{2i}]^2 \quad (1)$$

228 LNO_x mainly occurs via the NO₂+OH reaction:

$$LNO_x = k_{OH+NO_2+M}[OH][NO_2][M] \quad (2)$$

229 We calculate P(O₃) by subtracting the ozone loss pathways dictated by HO_x (HO+HO₂), NO₂+OH,
230 O₃ photolysis, ozonolysis, and the reaction of O(¹D) with water vapor from the formation pathways
231 through the removal of NO via HO₂ and RO₂:

$$P(O_3) = k_{HO_2+NO}[HO_2][NO] + \sum k_{RO_{2i}+NO}[RO_{2i}][NO] - k_{OH+NO_2+M}[OH][NO_2][M] - P(RONO_2) - k_{HO_2+O_3}[HO_2][O_3] - k_{OH+O_3}[OH][O_3] - k_{O(^1D)+H_2O}[O(^1D)][H_2O] - L(O_3) + \text{alkenes} \quad (3)$$

232 3. Results and Discussion

233 3.1. Box Model Validation

234 There are uncertainties associated with the box model (e.g., Brune et al., 2021; Zhang et
235 al., 2021; Lee et al., 2021) which can be attributed to: i) the lack of inclusion of physical processes
236 such as entrainment/detrainment, ii) discounting the heterogenous chemistry, iii) invalid
237 assumption of the diel steady state in areas close to large emission sources or in photochemically
238 less active environments (Thornton et al., 2002; Souri et al., 2021), iv) errors in the chemical
239 mechanism, and v) errors in the measurements. These limitations necessitate a thorough validation
240 of the model using unconstrained observations. While models have been known for a long time to
241 not be 100% accurate (Box, 1976), it is important to characterize whether the model can effectively
242 represent reality. For instance, if the simulated HCHO is poorly correlated with observations
243 and/or displayed large magnitude biases, it will be erroneous to assume that the sources of HCHO
244 along with relevant chemical pathways are appropriate.

245 We diagnose the performance of the box model by comparing the simulated values of five
246 compounds to observations: HCHO, NO, NO₂, PAN, hydroperoxyl radical (HO₂), and OH. Figure
247 2 depicts the scatterplot of the comparisons along with several statistics. HCHO observations are
248 usually constrained in box models to improve the representation of HO₂ (Schroeder et al., 2017;
249 Souri et al., 2020; Brune et al., 2021); however, this constraint may mask the realistic
250 characterization of the chemical mechanism with respect to the treatment of VOCs. Additionally,
251 it is important to know if the sources of HCHO are adequate. Therefore, we detach the model from
252 this constraint to carry out a more fair and stringent validation. Concerning HCHO, our model
253 does have considerable skill at reproducing the variability of observed HCHO (R²=0.73) with a
254 low bias of -4.9% (-0.09 ppbv). Likewise, the model performs well with regards to the simulation
255 of NO (R²=0.89) and NO₂ (R²=0.99) in the log scale. Immediately evident is the underestimation
256 of NO in highly polluted regions contrary to overestimation in clean ones. This discrepancy leads
257 to an underestimation (overestimation) of NO/NO₂ in polluted (clean) regions. The primary drivers
258 of NO/NO₂ are jNO₂ and O₃ both of which are constrained in the model. What can essentially
259 deviate the partitioning between NO and NO₂ from that of observations in polluted areas is the
260 assumption of the diel steady state which is rarely strictly valid where measurements are close to
261 large emitters. The overestimation of NO in low NO_x areas is often blamed on the lack of chemical



262 sink pathways of NO in chemical mechanism (e.g., Newland et al., 2021). A relatively reasonable
263 performance of PAN ($R^2=0.63$) is possibly due to constraining some of oxygenated VOCs such as
264 acetaldehyde. Xu et al. (2021) observed a strong dependency of PAN concentrations on NO/NO₂
265 ratios. Smaller NO/NO₂ ratios are usually associated with larger PAN because NO can effectively
266 remove peroxyacetyl radicals. We observe an overestimation of PAN (0.27 ppbv) possibly due to
267 an underestimation of NO/NO₂. Moreover, we should not rule out the impact of the first-order
268 dilution factor which was only empirically set in this study. For instance, if we ignore the dilution
269 process, the bias of the model in terms of PAN will increase by 33% resulting in a poor
270 performance ($R^2=0.40$) (not shown). Schroeder et al. (2020) found that proper simulation of PAN
271 in the polluted PBL during KORUS-AQ required a first-order loss rate based on thermal
272 decomposition at the average PBL temperature, which was more realistic than the widely varying
273 local PAN lifetimes associated with temperature gradients between the surface and the top of the
274 PBL. This solution is computationally equivalent to the dilution rate used in this study.

275 KORUS-AQ was the only field campaign providing OH and HO₂ measurements.
276 Concerning HO₂, former studies such as Schroeder et al. (2017), Souri et al. (2020), and Brune
277 et al. (2021) managed to reproduce HO₂ with R^2 ranging from 0.6 to 0.7. The performance of our
278 model ($R^2=0.66$) is similar to these past studies with near negligible biases (<1%). One may argue
279 that the absence of the HO₂ uptake by aerosols is contributing to some of the discrepancies we
280 observe in the HO₂ comparison. Brune et al. (2021) provided compelling evidence showing that
281 the consideration of the HO₂ uptake made their results significantly inconsistent with the
282 observations suggesting that the HO₂ uptake might have been inconsequential during the
283 campaign. Our model manages to reproduce 64% of the variance of observed OH outperforming
284 the simulations presented in Souri et al. (2020) and Brune et al. (2021) by >10%. The slope (= 1.03)
285 is not too far from the identity line indicating that our box model systematically overestimates
286 OH by $0.62 \cdot 10^6 \text{ cm}^{-3}$. This may be attributed to a missing OH sink in the mechanism or the lack
287 of inclusion of some VOCs. In general, the model performance is consistent, or outperforms,
288 results from recent box modelling studies which is an indication of it being at least virtually
289 representative of the real-world ozone chemistry and sensitivity regimes.

290 3.2. Can HCHO/NO₂ ratios fully describe the HO_x-RO_x cycle?

291 Kleinman et al. (2001) provided an analytical solution suggesting LRO_x/LNO_x is the most
292 robust ozone regime indicator. Thus, the predictive power of FNR at detecting the underlying
293 chemical conditions can be challenged by comparing FNR to LRO_x/LNO_x. Ideally, if they show
294 a strong degree of correspondence (i.e., $R^2=1.0$), we can confidently say that FNR can realistically
295 portray the chemical regimes. Any divergence of these two quantities is indicative of inadequacy
296 of the FNR indicator. Souri et al. (2020) observed a strong linear relationship between the
297 logarithmic transformed FNR and those of LRO_x/LNO_x. Our analysis in this study will be based
298 upon the simulated values to ensure that the relationship is coherent based on a realization from
299 the well-characterized box model. As pointed out by Schroeder et al. (2017) and Souri et al. (2020),
300 a natural logarithm of LRO_x/LNO_x roughly equal to -1.0 (i.e., LRO_x/LNO_x = 0.35-0.37)
301 perceptibly separates VOC-sensitive from NO_x-sensitive regimes, which would make this
302 threshold the baseline of our analysis.

303 Figure 3 demonstrates the log-log relationship of LRO_x/LNO_x and FNR, and P(O₃), from
304 all four air quality campaigns. The log-log relationships from each individual campaign are shown
305 in Figure S1-S4. We overlay the LRO_x/LNO_x baseline threshold along with two commonly used
306 thresholds for FNR suggested by Duncan et al. (2010); they defined the VOC-sensitive regimes if
307 FNR<1 and the NO_x-sensitive ones if FNR>2. Any region undergoing a value between these



308 thresholds is unlabeled and considered to be in a transitional regime. The size of each data point
309 is proportional to the $\text{HCHO} \times \text{NO}_2$ concentration magnitude. One striking finding from this plot is
310 that there is indeed a strong linear relationship between the logarithmic-transformed LROx/LNOx
311 and FNR ($R^2=0.91$). A strong linear relationship between the two quantities in the log-log scale is
312 indicative of a power law dependence (i.e., $y=ax^b$). A strong power law dependency means that
313 these two quantities have a poor correlation at their low and high values. This is mainly caused by
314 the fact that HCHO does not fully describe VOC reactivity rates in rich and poor VOC
315 environments (Souri et al., 2020). A question is what range of FNR will fall in $\ln(\text{LROx/LNOx}) =$
316 -1.0 ± 0.2 ? Following the baseline, the transitioning ratios follow a normal distribution with a mean
317 of 1.8, a standard deviation of 0.4, and a range from 1 to 4 (Figure S5). We define the chemical
318 error in the application of FNR to separate the chemical regimes as the relative error standard
319 deviation (i.e., σ/μ) of the transitioning ratios leading to $\sim 20\%$. These numbers are based on a
320 single model realization and can change if a different mechanism is used; nonetheless, the model
321 has considerable skill at reproducing many different unconstrained compounds, especially OH,
322 suggesting that it is a rather reliable realization. The comparison of the transitioning FNRs to the
323 NO_2 concentrations suggests no correlation ($r=0.02$) whereas there is a linear correlation between
324 the transitioning ratios and the HCHO concentrations ($r=0.56$). This tendency reinforces the study
325 of Souri et al. (2020) who, primarily due to the HCHO- NO_2 feedback, observed a larger FNR
326 threshold in VOC-rich environments to be able to detect the chemical regimes.

327 **3.3. Large PO_3 rates occur in regions with large $\text{HCHO} \times \text{NO}_2$ concentrations when** 328 **moving towards NOx -sensitive regions**

329 A striking and perhaps intuitive tendency observed from Figure 3 is that large PO_3 rates
330 are mostly tied to higher $\text{HCHO} \times \text{NO}_2$. But this relationship gradually weakens as we move
331 towards VOC-sensitive regions (smaller LROx/LNOx ratios). This is a textbook example of non-
332 linear ozone chemistry. In VOC-sensitive areas, PO_3 can be strongly inhibited by $\text{NO}_2 + \text{OH}$ and
333 the formation of organic nitrates despite the abundance of the precursors. In application of remote-
334 sensing of ozone precursors, the greatest unused metric describing the mass of the ozone precursors
335 is $\text{HCHO} \times \text{NO}_2$. However, this metric should only be used in conjunction with FNR. To
336 demonstrate this, based on what the baseline (LROx/LNOx) suggests against thresholds on FNRs
337 defined by Duncan et. al. (2010), we group the data into four regions namely as NOx -sensitive –
338 NOx -sensitive, NOx -sensitive–transitional, VOC-sensitive–transitional, and VOC-sensitive–
339 VOC-sensitive. A different perspective into this categorization is that the transitional regimes are
340 a weaker characterization of the main regime; for instance, NOx -sensitive–transitional regions are
341 less NOx -sensitive than NOx -sensitive – NOx -sensitive. Subsequently, the cumulative distribution
342 functions (CDFs) of PO_3 and $\text{HCHO} \times \text{NO}_2$ with respect to the aforementioned groups are
343 calculated, which is shown in Figure 4. Regarding NOx -sensitive— NOx -sensitive regions, we see
344 the PO_3 CDF very quickly converging to the probability of 100% indicating that the distribution
345 of PO_3 is skewed towards very low values. The median of PO_3 for this particular regime (where
346 $\text{CDF} = 50\%$) is only 0.25 ppbv/hr. This agrees with previous studies such as Martin et al. (2002),
347 Choi et al. (2012), Jin et al. (2017), and Souri et al. (2017) reporting that NOx -sensitive regimes
348 dominate in pristine areas. The PO_3 CDFs between NOx -sensitive—transitional and VOC-
349 sensitive—VOC-sensitive are not too distinct, whereas their $\text{HCHO} \times \text{NO}_2$ CDFs are substantially
350 different. The non-linear ozone chemistry suppresses PO_3 in highly VOC-sensitive areas such that
351 those values are not too different than those in mildly polluted areas (NOx -sensitive—transitional).
352 Perhaps the most interesting conclusion from this figure is that elevated PO_3 values (median = 4.6
353 ppbv/hr), a factor of two larger than two previous regimes, are mostly found in VOC-sensitive—



354 transitional. This is primary due to two causes: i) this particular regime is not strongly inhibited by
355 the nonlinear chemistry, particularly NO_2+OH , and ii) it is associated with abundant precursors
356 evident in the median of $\text{HCHO}\times\text{NO}_2$ being as three times as large of those in NO_x -sensitive—
357 transitional. This tendency illustrates the notion of the non-linear chemistry and how this may
358 affect regulations. Simply knowing where the regimes are might not suffice to pinpoint the peak
359 of PO_3 , as this analysis suggests that we need to take both FNR and $\text{HCHO}\times\text{NO}_2$ into
360 consideration; both metrics are readily accessible from satellite remote-sensing sensors.

361 3.4. *Can we estimate PO_3 using the information from HCHO/NO_2 and $\text{HCHO}\times\text{NO}_2$?*

362 It may be advantageous to construct an empirical function fitted to these two quantities and
363 elucidate the maximum variance (information) we can potentially gain to recreate PO_3 . After
364 several attempts, we found a bilinear function ($z=a_0+a_1x+a_2y+a_3xy$) to be a good fit without
365 overparameterization. Due to presence of extreme values in both FNR and $\text{HCHO}\times\text{NO}_2$, we use a
366 weighted least squares method for the curve fitting based on the distance of the fitted curve to the
367 data points (known as bi-squares weighting). The best fit with R^2 equals to 0.94 and an RMSE of
368 0.60 ppbv/hr is:

$$369 \text{PO}_3 = 0.74 - 0.09x - 0.02y + 0.25xy \quad (4)$$

369 where x and y are FNR (unitless) and $\text{HCHO}\times\text{NO}_2$ (ppbv²), respectively. The residual of the fit is
370 shown in Figure S6. The gradients of PO_3 with respect to x and y are:

$$\frac{d\text{PO}_3}{dx} = 0.25y - 0.09 \quad (5)$$

$$\frac{d\text{PO}_3}{dy} = 0.25x - 0.02 \quad (6)$$

371 An apparent observation arises from these equations that is the derivatives of PO_3 to each
372 metric depends on the other one underscoring their interconnectedness. For instance, Eq. (6)
373 suggests that larger FNRs (x) result in a larger gradient of PO_3 to the abundance of $\text{HCHO}\times\text{NO}_2$
374 (y). In very low FNRs, this gradient can become very small rendering PO_3 insensitive (or in
375 extreme cases, negatively correlated) to $\text{HCHO}\times\text{NO}_2$. This analysis provides encouraging results
376 about the future application of the satellite-derived $\text{HCHO}\times\text{NO}_2$; however, the wide class of
377 problems relating to the application of satellite-derived FNR columns such as satellite errors in
378 columns or the translation between columns to PBL are also present in Eq. (4), even in a more
379 pronounced way due to $\text{HCHO}\times\text{NO}_2$ and $\text{HCHO}^2 (=xy)$. This new perspective into PO_3 estimation
380 deserves a separate study.

381 3.5. *Altitude dependency and its parametrization*

382 A lingering concern over the application of satellite-based FNR tropospheric columns is
383 that the vertical distribution of HCHO and NO_2 are integrated in columns thus this vertical
384 information is permanently lost. As such, here we provide insights on the vertical distribution of
385 FNR within the tropospheric column. This task requires information about the differences between
386 the vertical shape of HCHO and that of NO_2 . Ideally, if both compounds show an identically
387 relative shape, the FNR columns will be valid for every air parcel along the vertical path (i.e., a
388 straight line). We do not always know the precise knowledge of HCHO and NO_2 vertical
389 distributions, but we can constitute some degree of generalizations by leveraging the
390 measurements made during the aircraft campaigns.

391 Figure 5 demonstrates the violin plot of the afternoon ($> 12:00$ LST) vertical distribution
392 of HCHO , NO_2 , and FNR observed by NASA's aircrafts during the four field campaigns analyzed
393 in this study superimposed by the simulated PO_3 rates. The vertical layers are grouped into sixteen



394 altitudes ranging from 0.25 km to 7.75 km. Each vertical layer incorporates measurements ± 0.25
395 km of the altitude mid-layer height. The observations do not follow a normal distribution,
396 particularly in the lower parts of the atmosphere; thus medians are preferred to represent the central
397 tendency. While the largest PO_3 rates tend to occur in areas close to the surface (< 2 km agl), a
398 nonnegligible fraction of the elevated PO_3 rates are also observed in other parts of the atmosphere
399 such as those in the free troposphere.

400 Several intriguing features are observed from Figure 5: First, up to the 5.75 km range,
401 which encompasses the PBL area and a large portion of the free-troposphere, NO_2 concentrations
402 tend to decrease quicker than those of HCHO in line with previous studies such as Schroeder et al.
403 (2017), Jin et al. (2017), Chan et al. (2019), and Ren et al. (2022). Second, above 5.75 km, HCHO
404 continues to decrease whereas NO_2 shows an increasing trend. As a result of their different vertical
405 trends, we observe nonuniformities in the vertical distribution of FNR: they become more NO_x -
406 sensitive with altitude up to a turning point at 5.75 km and then shift backwards to VOC-sensitive.

407 It is attractive to model these shapes and apply parameterizations to understand how their
408 shapes will complicate the use of tropospheric column retrieval from satellites. First order rational
409 functions are a good candidate to use. Concerning the vertical dependency of HCHO and NO_2 , we
410 find reasonable fit ($R^2=0.73$) as:

$$HCHO, NO_2 = \frac{a_0 z + a_1}{z + a_2} \quad (7)$$

411 where z is altitude in km. a_i ($i=0,1,2$) are fitting parameters. From this equation it is determined
412 that FNRs follow a second order rational function:

$$f(z) = \frac{HCHO}{NO_2} = \frac{b_0 z^2 + b_1 z + b_2}{b_3 z^2 + b_4 z + b_5} \quad (8)$$

413 where b_i ($i=0, \dots, 5$) are fitting parameters. One can effortlessly fit this function to different bounds
414 of the vertical distribution of FNR such as the 25th and 75th percentiles, and subsequently estimate
415 the first moment of the resultant polygon along z via:

$$\left. \frac{HCHO}{NO_2} \right|_{z_1}^{z_2} = \frac{1}{2A} \int_{z_1}^{z_2} f^2(z)_{75th} - f^2(z)_{25th} \quad (9)$$

416 where A is the area of the polygon bounded by the 75th percentiles, $f(z)_{75th}$, and the 25th
417 percentiles ($f(z)_{25th}$) of FNR (shown in Figure 5 as solid black lines). We define an altitude
418 adjustment factor (f_{adj}) such that one can translate an observed FNR tropospheric column ratios,
419 such as those retrieved from satellites, to a defined altitude and below that point (zt) through:

$$f_{adj} = \frac{\left. \frac{HCHO}{NO_2} \right|_0^{zt}}{\left. \frac{HCHO}{NO_2} \right|_0^{8 km}} \quad (10)$$

420 where zt can be interchanged to match the PBLH. This definition is more beneficial than using the
421 entire tropospheric column to the surface conversion (e.g., Jin et al., 2017) because ozone can be
422 formed in various vertical layers. Using the observations collected during the campaign, we
423 estimate Eq. (10) along with $\pm 1\sigma$ boundaries shown in Figure 6. The shape of the resulting
424 adjustment factor is in line with of the vertical distribution of FNR (see Figure 5): the adjustment
425 factor curve closer to the surface have values smaller than one, increases to values larger than one
426 in the mid-troposphere, and finally converges to one near the top of the tropospheric column. If
427 one picks out an altitude pertaining to a PBLH, they can easily apply f_{adj} to the observed FNR
428 columns to estimate the corresponding ratio for that specific PBLH. A more evolved PBLH (i.e.,



429 a large z_t) results in stronger vertical mixing rendering f_{adj} closer to one. The standard error
430 deviation of this conversion is around 26%.

431 It is beneficial to model this curve to make this data-driven conversion easier for future
432 applications. A second-order polynomial can well describe ($R^2=0.99$) this curve:

$$f_{\text{adj}} = az_t^2 + bz_t + c \quad a = -0.02, b = 0.25, c = 0.41 \quad (11)$$

433 Although Eq. (11) does not include observations above 8 km, the area bounded between $f(z)_{75\text{th}}$
434 and $f(z)_{25\text{th}}$ in higher altitudes is too small to make a noticeable impact on this adjustment factor.

435 One may object that since we estimated the adjustment factor based on two boundaries
436 (25th and 75th percentiles) of the data we are no longer really dealing with 50% of features observed
437 in the vertical shapes of FNR. This valid critique can be overcome by gradually relaxing the lower
438 and upper limits and examine the resulting change in f_{adj} . When we reduce the lower limit in Eq.
439 (9) from the 25th to 1st percentiles the optimal curve is similar to the one shown in Figure 6 (Figure
440 S7). However, when we extend the upper limit from 75th percentiles to greater values, we see the
441 fit becoming less robust above the 80th percentiles indicating that the formulation is applicable for
442 ~80% of the data. The reason behind the poor representation of the adjustment factor for the upper
443 tail of the population is the extremely steep turning point between 5.5 and 6.0 km necessitating a
444 higher order rational function to be used for Eq. (7) and Eq. (8). We prefer to limit this analysis to
445 both boundaries and the order defined in Eq. (8) and Eq. (9) because extreme value predictions
446 usually lack robustness.

447 A caution with these results is that our analysis is limited to afternoon observations because
448 our focus is on afternoon low orbiting sensors such as OMI and TROPOMI. Nonetheless,
449 Schroeder et al. (2017) and Crawford et al. (2021) observed a large diurnal variability in these
450 profiles due to diurnal variability in sinks and sources of NO_2 and HCHO, and atmospheric
451 dynamics. The diurnal cycle has indeed an important implication for geostationary satellites such
452 as Tropospheric Emissions: Monitoring of Pollution (TEMPO) (Chance et al., 2019).

453 Another important caveat with our analysis is that it is based upon four air quality
454 campaigns taking place in warm seasons avoiding times/areas with convective transport; as such
455 our analysis is ignorant about the vertical shapes of FNR during convective activities and cold
456 seasons. These oversights can be downplayed by a few compelling assumptions: first, it is very
457 atypical to encounter elevated ozone production rates during cold seasons with few exceptions
458 (Ahmadov et al., 2015; Rappenglück et al., 2014); second, the notion of ozone regimes is only
459 appropriate in photochemically active environments where the ROx-HOx cycle is active; an
460 example of this can be found in Souri et al. (2021) who observed an enhancement of surface ozone
461 in central Europe during a lockdown in April 2020 (up to 5 ppbv) compared to a baseline which
462 was explainable by the reduced O_3 titration through NO in place of the photochemically induced
463 production. An exaggerated extension to this example is the nighttime chemistry where NO- O_3 -
464 NO_2 partitioning is the major driver of negative ozone production rates; at night, the definition of
465 NOx-sensitive or VOC-sensitive is meaningless, so is in photochemically less active
466 environments; third, it is rarely advisable to use cloudy scenes in satellite UV-Vis gas retrievals
467 due to the arguable assumption on Lambertian clouds and highly uncertain cloud optical centroid
468 and albedo; accordingly, convection occurring during storms or fires are commonly masked in
469 satellite-based studies. Therefore, the limitations associated with the adjustment factor are mild
470 compared to the advantages.



471 3.6. Spatial Heterogeneity

472 The spatial representation error resulting from both unresolved processes and scales (Janić
473 et al., 2016; Valin et al., 2011; Souri et al., 2022) refers to the procedure of the quantification of
474 the amount of information lost due to satellite footprint or unresolved inputs used in satellite
475 retrieval algorithms. This source of error cannot be determined when we do not know the true state
476 of the spatial variability. There is, however, a practical way to determine this by conducting multi-
477 scale intercomparisons of a coarse spatial resolution output against a finer one. Yet, despite the
478 absence of the truth in this approach, we tend to find their comparisons useful in giving us an
479 appreciation of the error.

480 We build the reference data on qualified pixels ($qa_value > 0.75$) of offline TROPOMI
481 tropospheric NO_2 version 2.2.0 (van Geffen et al., 2021; Boersma et al., 2018) and total HCHO
482 columns version 2.02.01 (De Smedt et al., 2018) oversampled at $3 \times 3 \text{ km}^2$ in summer 2021 over
483 the US. Figure 7 shows the map of those tropospheric columns as well as FNR. Encouragingly,
484 the small footprint and relatively low detection limit of TROPOMI compared to its predecessor
485 satellite sensors (e.g., OMI) enables us to have possibly one of the finest maps of HCHO over the
486 US to date. Large values of HCHO columns are found in the southeast due to strong isoprene
487 emissions (e.g., Zhu et al., 2016; Wells et al., 2020). Cities like Houston (Boeke et al., 2011; Zhu
488 et al., 2014; Pan et al., 2015; Diao et al., 2016), Kansas City, Phoenix (Nunnermacker et al., 2004),
489 and Los Angeles (de Gouw et al., 2018) also show pronounced enhancements of HCHO possibly
490 due to anthropogenic sources. Expectedly, large tropospheric NO_2 columns are often confined to
491 cities and some coal-fired power plants along Ohio river basin. Concerning FNR, low values
492 dominate cities whereas high values are found in remote regions. An immediate tendency observed
493 from these maps is that the length scale of HCHO columns is longer than that of NO_2 . This
494 indicates that NO_2 columns are more heterogenous. It is because of this reason that we observe a
495 large degree of the spatial heterogeneity with respect to FNRs.

496 Here we limit our analysis to Los Angeles due to computational costs imposed by the
497 subsequent experiment. To quantify the spatial representation errors caused by satellite footprint
498 size, we upscale the FNRs by convolving the values with four low pass box filters with the size of
499 13×24 , 36×36 , 108×108 , and $216 \times 216 \text{ km}^2$, shown in the first column of Figure 8. Subsequently,
500 to extract the spatial variance (information), we follow the definition of the experimental
501 semivariogram (Matheron, 1963):

$$\gamma(\mathbf{h}) = \frac{1}{2N(\mathbf{h})} \sum_{|x_i - x_j| - |\mathbf{h}| \leq \varepsilon} [Z(x_i) - Z(x_j)]^2 \quad (12)$$

502 where $Z(x_i)$ (and $Z(x_j)$) is discrete pixels of FNRs, $N(\mathbf{h})$ is the number of paired pixels separated
503 by the vector of \mathbf{h} . $|\cdot|$ operator indicates the length of a vector. The condition of $|x_i - x_j| - |\mathbf{h}| \leq$
504 ε is to permit certain tolerance for differences in the length of the vector. Here, we rule out the
505 directional dependency in $\gamma(\mathbf{h})$, which in turn, makes the vector of \mathbf{h} scalar ($h = |\mathbf{h}|$). Moreover,
506 we bin γ values in 100 evenly-spaced intervals ranging from 0 to 5 degree. To model the
507 semivariogram, we follow the stable Gaussian function used in Souri et al. (2022):

$$\gamma(h) = s(1 - e^{-\left(\frac{h}{r}\right)^{c_0}}); c_0=1.5 \quad (13)$$

508 where r and s are fitting parameters. For the most part, geophysical quantities become spatially
509 uncorrelated at a certain distance called the range and the variance associated with that distance is
510 called the sill. that the fitting parameters r and s describe these two quantities as long as the stable



511 Gaussian function can well fit to the shape of semivariogram. The semivariograms, and the fits,
512 associated with each map is depicted in the second column of Figure 8.

513 The modeled semivariograms suggest that a coarser field comes with a smaller sill,
514 implying a loss in the spatial information (variance). The length scale (i.e., the range) only sharply
515 increases at coarser footprints ($>36\times36$ km²). This indicates that several coarse resolution satellite
516 sensors such as OMI (13×24 km²) are rather able to determine the length scales of FNR over a
517 major city such as Los Angeles. By leveraging the modeled semivariograms, we can effortlessly
518 determine the spatial representation error for specific scale (e.g., $h=10$ km) through

$$e^2(h) = 1 - \frac{\gamma(h)}{\gamma_{ref}(h)} \quad (14)$$

519 where $\gamma_{ref}(h)$ is the modeled semivariogram of the reference field (3×3 km²). Figure 9 shows the
520 spatial representation errors for different fields and different length scales. For the most part, the
521 OMI nadir pixel (13×24 km²) only have a ~12% loss of the spatial variance. On the contrary, a
522 grid box with a size of 216×216 km² fails at capturing ~65% of the spatial information in FNR
523 with a 50 km length scale comparable to the extent of Los Angeles. The advantage of our method
524 is that we can mathematically describe the spatial representation error as function of the length of
525 our target. The present method can be easily applied to other atmospheric compounds and
526 locations. We have named this method SpaTial Representation Error EstimaTor (STREET) which
527 is publicly available as an open-source package (<https://github.com/ahsouri/STREET>, Last
528 Access, May 31, 2022).

529 An oversight in the above experiment lies in its lack of appreciation of unresolved physical
530 processes in the satellite measurements: weaker sensitivity of some spectra windows to the near-
531 surface pollution (Yang et al., 2014), using 1-D air mass factor calculation instead of 3-D
532 (Schwaerzel et al., 2020), and discounting aerosol effect on the light path are just few examples to
533 point out. To account for the unresolved processes, one can recalculate Eqs. (12)-(14) using outputs
534 coming from different retrieval frameworks, which is beyond the scope of this study.

535 3.7. Satellite errors

536 3.7.1. Concept

537 Two types of retrieval errors can affect our analysis: systematic errors (bias) and
538 unsystematic ones (random errors). In theory, it is very compelling to understand their differences.
539 In reality, the distinction between random and systematic errors is not as clear-cut as it seems. One
540 may wish to establish the credibility of a satellite retrieval by comparing it to a sky-radiance
541 measurement over time. Because each measurement is made at a different time, their comparison
542 is not a repetition of the same experiment; each time, the atmosphere differs in some aspects so
543 each comparison is unique. Adding more sky-radiance measurements will simply add new
544 experiments. For each paired data points, there are many unique issues contributing differently to
545 errors; as such our problem is grossly under-determined (i.e., more unknowns for a given
546 observation). Here, we do not attempt to separate those types of errors in the subsequent analysis,
547 thereby limiting the analysis to the total uncertainty.

548 We focus on analyzing the statistical errors drawn from the differences between benchmark
549 and the retrievals on daily basis. Two sensors are used for this analysis: TROPOMI and OMI. To
550 propagate individual uncertainties in HCHO and NO₂ to FNRs, we follow an analytical approach
551 involving Jacobians of the ratio to HCHO and NO₂. Assuming that errors in HCHO and NO₂ are
552 uncorrelated, the relative error of the ratio can be estimated by:



$$\frac{\sigma}{ratio} = \sqrt{\left(\frac{\sigma_{HCHO}}{HCHO}\right)^2 + \left(\frac{\sigma_{NO_2}}{NO_2}\right)^2} \quad (15)$$

553 where σ_{HCHO} and σ_{NO_2} are total uncertainties of HCHO and NO_2 observations.

554 3.7.2. Error Distributions in TROPOMI and OMI

555 We begin our analysis with the error distribution of daily TROPOMI tropospheric NO_2
556 columns (v1.02.02) against 22 MAX-DOAS instruments from May to Sep in 2018-2021. The data
557 are paired based on the criteria defined in Verhoelst et al. (2021). The list of stations and the
558 number of available days for each are mapped in Figure S8. Figure 10a shows the histogram of the
559 TROPOMI minus the MAX-DOAS instruments. The first observation from this distribution is that
560 it is skewed towards lower differences evident in the skewness parameter around -4.6. As a result
561 of the skewness, the median should be a better representative of the central tendency which is
562 around -1×10^{15} molec./ cm^2 . In general, TROPOMI tropospheric NO_2 columns show a low bias.
563 We fit a normal distribution to the data using non-linear Levenberg-Marquardt method. This fitted
564 normal distribution ($R^2=0.94$) is used to approximate σ_{NO_2} for different confidence intervals and
565 to play down blunders.

566 The error analysis for OMI follows the same methods applied for TROPOMI; however,
567 with different benchmarks. We follow the comparisons made between the operational product
568 version 3.1 and measured columns derived from NCAR's NO_2 measurements integrated along
569 aircraft spirals during four NASA's air quality campaigns. More information regarding this data
570 comparison can be found in Choi et al. (2020). Figure 10b shows the histogram of OMI minus the
571 integrated spirals. Compared to TROPOMI, the OMI bias is worse by a factor of two. The standard
572 deviation calculated from a Gaussian fit (2.31×10^{15} molec./ cm^2) is not substantially different than
573 that of TROPOMI (2.11×10^{15} molec./ cm^2).

574 As for the error distribution of TROPOMI HCHO columns (version 1.1.(5-7)), we use 24
575 FTIR measurements during the same time period based on the criteria specified in Vigouroux et
576 al. (2020). The stations along with their number of available data are mapped in Figure S8. The
577 frequency of the paired data is daily. Figure 11a depicts the error distribution. The distribution is
578 slightly broader compared to that of NO_2 , manifested in a larger standard deviation 4.32×10^{15}
579 molec./ cm^2 . This is primarily due to the fact that the molecular absorption of HCHO is much
580 smaller/narrower than that of NO_2 in the UV-Vis range (Gonzalez Abad et al., 2019);
581 consequently, HCHO observations are more contaminated by noise. Similar to the NO_2 , we fit a
582 normal distribution ($R^2=0.90$) to specify σ_{HCHO} for different confidence intervals.

583 Concerning OMI HCHO columns from SAO version 3 (Gonzalez Abad et al., 2015), we
584 follow the intercomparison approach proposed in Zhu et al. (2020). Based on this approach, the
585 benchmarks come from GEOS-Chem simulated HCHO columns corrected by in-situ aircraft
586 measurements. The measurements were made during ozone seasons from KORUS-AQ,
587 DISCOVERs, FRAPPE, NOMADSS, and SENEX campaigns (see Table 1 in Zhu et al. 2020).
588 OMI values ranging from -0.5×10^{15} molec./ cm^2 and 1.0×10^{17} molec./ cm^2 with effective cloud
589 fraction between 0.0 and 0.3, and SZA between 0 and 60 degrees are only considered in the
590 comparison. Any pixels from OMI and grid boxes from the corrected GEOS-Chem simulation that
591 fall into a polygon enclosing the campaign domain are used to create the error distribution shown
592 in Figure 11b. The distribution has much denser data because the model output covers a large
593 portion of the satellite swath. The error distribution suggests that OMI HCHO is inferior to
594 TROPOMI evident in larger bias and standard deviation. The OMI bias is twice as large as that of



595 TROPOMI. De Smedt et al. (2021) observed the same level of bias from their comparisons of
596 OMI/TROPOMI with MAX-DOAS instruments (see Table 3 in their paper). Moreover, their OMI
597 vs MAX-DOAS comparisons were severely scattered. Likewise, we observe the standard deviation
598 of OMI from the fitted Gaussian function to be roughly five times as large of that TROPOMI. This
599 can primarily due to a weaker signal-to-noise (and sensor degradation) in OMI. It is because of
600 this reason that OMI HCHO should be oversampled for few months. Another possible reason for
601 the large standard deviation is the fact that the benchmark arises from a modeling experiment
602 whose ability at resolving spatiotemporal variations in HCHO may be uncertain. This partly leads
603 to the performance of OMI to look poor.

604 3.7.3. *The impact of retrieval error on the ratio*

605 Following Eq. (15), we calculate the standard error for a wide range of NO₂ and HCHO
606 columns at three confidence intervals based on the standard deviation derived from the fitted
607 Gaussian function to the histograms. The resultant standard error (%) at 68% confidence interval
608 (1 sigma) for both TROPOMI and OMI is shown in Figure 12. We observe smaller errors to be
609 associated with larger tropospheric column concentrations. As for TROPOMI, either daily HCHO
610 or tropospheric NO₂ columns should be above 1.2-1.5×10¹⁶ molec./cm² to achieve 20-30%
611 standard error. The TROPOMI errors start diminishing the application of FNR when both
612 measurements are below this threshold. Regarding OMI, it is nearly impossible to get the standard
613 error below of 20-30% given its problematically large HCHO standard deviation. For 50% error,
614 the daily HCHO columns should be above 3.2×10¹⁶ molec./cm². This range of error can also be
615 achieved if OMI tropospheric NO₂ columns are above 8×10¹⁵ molec./cm².

616 3.8. *The fractional errors to the total error*

617 The ultimate task is to compile the aforementioned errors to gauge how each individual
618 source of error contributes to the overall error. The overall error is given by:

$$\sigma_{total} = \sqrt{\sigma_{Col2PBL}^2 + \sigma_{SpatialRep}^2 + \sigma_{Retrieval}^2} \quad (16)$$

619 $\sigma_{Col2PBL}$ is the error in the adjustment-factor defined in this study. We calculated a 26% standard
620 error for a wide range of PBLHs. Therefore, $\sigma_{Col2PBL}$ equals to 26% of the observed ratio (i.e.,
621 magnitude dependent). $\sigma_{SpatialRep}$ is more complex. It is a function of the footprint of the satellite
622 (or a model), the spatial variability of the reference field which varies from environment to
623 environment, and the length scale of our target (e.g., a district, a city, or a state). Eq. (14) explicitly
624 quantifies this error. The product of the square root of that value and the observed ratio defines
625 $\sigma_{SpatialRep}$. The last error depends on the magnitude of HCHO and NO₂ tropospheric columns. It
626 can be estimated from Eq. (15) times the observed ratio. We did not include the chemistry error in
627 Eq. (16) because it was suited only for segregating the chemical conditions; it does not describe
628 the level of uncertainties that comes with the observed columnar ratio. Figure 13 shows the total
629 relative error given the observed TROPOMI ratio seen in Figure 7. We consider the OMI spatial
630 representation error (13% variance loss) for this case that was computed in a city environment.
631 The retrieval errors are based on TROPOMI sigma values. Areas associated with relatively small
632 errors (<50%) are mostly seen in cities due to a stronger signal (smaller $\sigma_{Retrieval}$). Places with
633 low vegetation and anthropogenic sources (i.e., Rocky Mountains) possess the largest errors
634 (>100%).

635 To produce some examples of the fractional errors to the total error, we focus on two
636 different environments with two different sets of HCHO and NO₂ columns. One represents a



637 heavily polluted area, and the other one a moderately polluted region. We also include two
638 footprints: OMI ($13 \times 24 \text{ km}^2$) and a $108 \times 108 \text{ km}^2$ pixel. Finally, we calculate the percentage of
639 each error component for both OMI and TROPOMI sensors. Figure 14 shows the pie charts
640 describing the percentage of each individual error to the total error for TROPOMI. Unless the
641 footprint of the sensor is coarse enough (e.g., 108 km^2) to give rise to the spatial representation
642 error dominance, the retrieval error stands out. It is not expected for new satellites to have very
643 large footprints; as such, the retrieval errors appear to be the major obstacle for using FNR in a
644 robust manner. Figure 15 shows the same calculation but using OMI errors; the retrieval errors
645 massively surpass other errors. This motivates us to do one more experiment; we recalculate the
646 HCHO error distribution in OMI using monthly-averaged data instead of daily (Figure S9). This
647 experiment suggests a standard deviation of $9.4 \times 10^{15} \text{ molec./cm}^2$ with which we again observe
648 the retrieval error to be the largest contributor ($>80\%$) of the total error (Figure S10).

649 4. Summary

650 The main goal of this study was to characterize the errors associated with the ratio of
651 satellite-based HCHO to NO_2 columns which has been widely used for ozone sensitivity studies.
652 From the realization of the complexity of the problem we now know that four major errors should
653 be carefully quantified so that we can reliably represent the underlying ozone regimes. The errors
654 are broken down into i) the chemistry error, ii) the column to the PBL translation, iii) the spatial
655 representation error, and iv) the retrieval error. Each error has its own dynamics and has been
656 tackled differently by leveraging a broad spectrum of tools and data.

657 The chemistry error refers to the predictive power of HCHO/ NO_2 ratio (hereafter FNR) at
658 describing the HO_x-RO_x cycle which can be well explained by the ratio of the chemical loss of
659 HO₂+RO₂ (LRO_x) to the chemical loss of NO_x (LNO_x). Because those chemical reactions are not
660 directly observable, we set up a chemical box model constrained with a large suite of in-situ aircraft
661 measurements collected during DISCOVER-AQs and KORUS-AQ campaigns (~ 500 hr of flight).
662 Our box model showed a reasonable performance at recreating some of unconstrained key
663 compounds such as OH ($R^2=0.64$, bias=17%), HO₂ ($R^2=0.66$, bias<1%), and HCHO ($R^2=0.73$,
664 bias=5%). Subsequently we compared the simulated FNRs to LRO_x/LNO_x. They showed a high
665 degree of correspondence ($R^2=0.93$) but only in the log-log scale; this indicated that FNRs poorly
666 described the HO_x-RO_x cycle for heavily polluted environments as well as pristine ones.
667 Following a robust baseline indicator ($\ln(\text{LRO}_x/\text{LNO}_x) = -1.0 \pm 0.2$) segregating NO_x-sensitive
668 from VOC-sensitive regimes, we observed a diverse range of FNR ranging from 1 to 4. These
669 transitioning ratios had a Gaussian distribution with a mean of 1.8 and standard deviation of 0.4.
670 This implied that the relative standard error associated with the ratio from the chemistry
671 perspective at 68% confidence interval was 20%. Although this threshold with its error was based
672 on a single model realization and can be different for a different chemical mechanism, it provided
673 a useful universal baseline derived from various chemical and meteorological conditions. At 68%
674 confidence level, any uncertainty beyond 20% in the ozone regime identification from FNRs likely
675 originates from other sources of error such as the retrieval error.

676 Results from the box model showed that ozone production rates in extremely polluted
677 regions (VOC-sensitive) were not significantly different than those in pristine ones (NO_x-
678 sensitive) due to non-linear chemical feedback mostly imposed by NO₂+OH. Indeed, the largest
679 PO₃ rates (median = 4.6 ppbv/hr) were predominantly seen in VOC-sensitive regimes tending
680 towards the transitional regime. This was primary caused by the abundance of ozone precursors
681 (i.e., HCHO×NO₂) in addition to the diminished negative chemical feedback. We also revealed
682 that HCHO×NO₂ can be used as a sensible proxy for the ozone precursors abundance. In theory,



683 this metric in conjunction with the ratio provided reasonable estimates on PO_3 rates (± 0.60
684 ppbv/hr).

685 We then analyzed the afternoon vertical distribution of HCHO, NO_2 , and their ratio
686 observed from aircrafts during the air quality campaigns binned to the near surface to 8 km. For
687 altitudes below 5.75 km, HCHO concentration steadily decreased with altitude but at a smaller rate
688 compared to NO_2 . Above that altitude, NO_2 concentrations stabilized and slightly increased due to
689 lightning and stratospheric sources. The dissimilarity between the vertical shape of NO_2 versus
690 HCHO resulted in a non-linear shape of FNR. This non-linear shape necessitated a mathematical
691 formulation to transform an observed columnar ratio to a ratio at a desired vertical height
692 expanding from the surface. We fit a second-order rational function to the profile and formulated
693 the altitude adjustment factor which clearly followed a second-order polynomial function starting
694 from values below 1 for lower altitudes, following values above 1 for some high altitudes, and
695 finally converging to 1 at 8 km. This behavior means that for a given tropospheric columnar ratio,
696 the ozone regime tends to get pushed towards the VOC-sensitive regime near the surface. This
697 data-driven adjustment factor exclusively derived from afternoon aircraft profiles during warm
698 seasons in non-convective conditions had a standard error of 26%.

699 An important error in the satellite-based observations stemmed from unresolved spatial
700 variability in trace gas concentrations within a satellite pixel (Souri et al., 2022; Tang et al., 2021).
701 The amount of unresolved spatial variability (the spatial representation error) can in principle be
702 modeled if we base our reference on a distribution map made from a high spatial resolution dataset.
703 We modeled semivariograms (or spatial auto-correlation) computed for a reference map of FNR
704 observed by TROPOMI at $3 \times 3 \text{ km}^2$ over Los Angeles. Subsequently, we coarsened the map to
705 13×24 , 36×36 , 108×108 , and $216 \times 216 \text{ km}^2$ and modeled their semivariograms. As for $13 \times 24 \text{ km}^2$,
706 which is equivalent of the OMI nadir spatial resolution, around 12% of spatial information
707 (variance) was lost due to its footprint. The larger the footprint, the bigger spatial representation
708 error. For instance, a grid box with the size of $216 \times 216 \text{ km}^2$ lost 65% of the spatial information in
709 the ratio at 50 km length scale. Our method is compelling to understand and easy to apply for other
710 products and different atmospheric environments. We developed an open-source package called
711 SpaTial Representation Error EstimaTor (STREET) (<https://github.com/ahsouri/STREET>) based
712 on this approach.

713 We presented estimates of retrieval errors associated with daily TROPOMI and OMI
714 tropospheric NO_2 columns by comparing them against a large suite of MAX-DOAS (Verhoelst et
715 al. 2021) and vertically-integrated measurements from aircraft spirals (Choi et al., 2020). Both
716 products were smaller than the benchmark. Furthermore, they show a relatively consistent
717 dispersion at 68% confidence level ($\sim 2 \times 10^{15} \text{ molec./cm}^2$) suggested by fitting a normal function
718 ($R^2 > 0.9$) to their error distributions. As for daily TROPOMI and OMI HCHO products, we used
719 global FTIR observations (Vigouroux et al., 2020) and data-constrained GEOS-Chem outputs from
720 multiple campaigns (Zhu et al., 2020), respectively. TROPOMI HCHO indeed outperforms OMI
721 HCHO with respect to bias and dispersion on a daily basis. The standard deviation of OMI HCHO
722 was found to be roughly five times as large compared to TROPOMI. While this error can be partly
723 reduced by oversampling over a span of a month or a season, it is critical to recognize that ozone
724 events are episodic, thus daily observations should be the standard mean for understanding the
725 chemical pathways for the formation of surface ozone. After combining the daily biases from both
726 HCHO and NO_2 TROPOMI comparisons, we came to the conclusion that either daily HCHO or
727 tropospheric NO_2 columns should be above $1.2\text{--}1.5 \times 10^{16} \text{ molec./cm}^2$ to achieve 20-30% standard
728 error in the ratio. Due to the large error in daily OMI HCHO, it was nearly impossible to achieve



729 20-30% standard error given the observable range of HCHO and NO₂ columns over our planet. To
730 reach to 50% error using daily OMI data, either HCHO columns should be above 3.2×10^{16}
731 molec./cm² or tropospheric NO₂ columns should be above 8×10^{15} molec./cm².

732 We finally calculated the total error in the ratio by combining the TROPOMI retrieval
733 errors, the spatial representation error pertaining to OMI nadir footprint over a city-like
734 environment, and the altitude adjustment error for a wide range of observed HCHO and NO₂
735 columns over the US. These observations were based on the TROPOMI in summertime 2021. The
736 total errors were relatively mild (<50%) in cities due to a stronger signal, whereas they easily
737 exceeded 100% in regions with low vegetation and anthropogenic sources (i.e., Rocky Mountains).
738 The dominant source of the total error (40-90%) was the retrieval error.

739 All of these aspects highlight the necessity of improving the trace gas satellite retrieval
740 algorithms in conjunction with sensor calibration, although with the realization that a better
741 retrieval is somewhat limited by the advancements made in other disciplines such as atmospheric
742 modeling and molecular spectroscopy.

743 **Acknowledgment**

744 This study was funded by NASA's Aura Science Team (grant number: 80NSSC21K1333). PTR-
745 MS measurements were supported by the Austrian Federal Ministry for Transport, Innovation and
746 Technology (bmvit, FFG-ALR-ASAP). The PTR-MS instrument team (P. Eichler, L. Kaser, T.
747 Mikoviny, M. Müller) is acknowledged for their support with field work and data processing. We
748 acknowledge FTIR HCHO measurements team including T. Blumenstock, M. Grutter, J. W.
749 Hannigan, N. Jones, R. Kivi, E. Lutsch, E. Mahieu, M. Makarova, I. Morino, I. Murata, T.
750 Nagahama, J. Notholt, I. Ortega, M. Palm, A. Röhlings, M. Schneider, D. Smale, W. Stremme, K.
751 Strong, Y. Sun, R. Sussmann, Y. Té, and P. Wang. The measurements at Paramaribo have been
752 supported by the BMBF (German Ministry of Education and Research) in the project ROMIC-II
753 subproject TroStra (01LG1904A). We thank the Meteorological Service Suriname and Cornelis
754 Becker for support. The measurements and data analysis at Bremen are supported by the Senate of
755 Bremen. The NCAR FTS observation programs at Thule, GR, Boulder, CO and Mauna Loa, HI
756 are supported under contract by the National Aeronautics and Space Administration (NASA). The
757 National Center for Atmospheric Research is sponsored by the National Science Foundation. The
758 Thule effort is also supported by the NSF Office of Polar Programs (OPP). Operations at the
759 Rikubetsu and Tsukuba FTIR sites are supported in part by the GOSAT series project. The Paris
760 TCCON site has received funding from Sorbonne Université, the French research center CNRS
761 and the French space agency CNES. The Jungfraujoch FTIR data are primarily available thanks to
762 the support provided by the F.R.S. - FNRS (Brussels), the GAW-CH program of MeteoSwiss
763 (Zürich) and the HFSJG.ch Foundation (Bern). The MAX-DOAS data used in this publication
764 were obtained from A. Bais, J. Burrows, K. Chan, M. Grutter, C. Liu, H. Irie, V. Kumar, Y.
765 Kanaya, A. Piters, C. Rivera-Cárdenas, M. Van Roozendaal, R. Ryan, V. Sinha, and T. Wagner.
766 Fast delivery of MAX-DOAS data tailored to the S5P validation was organized through the S5PVT
767 AO project NIDFORVAL. IUP-Bremen ground-based measurements are funded by DLR-Bonn
768 received through project 50EE1709A. We thank the IISER Mohali atmospheric chemistry facility
769 for supporting the MAX-DOAS measurements at Mohali, India. KNMI ground-based
770 measurements in De Bilt and Cabauw are partly supported by the Ruisdael Observatory project,
771 Dutch Research Council (NWO) contract 184.034.015, by the Netherlands Space Office (NSO)
772 for Sentinel-5p/TROPOMI validation, and by ESA via the EU CAMS-27 project. LZ and SS
773 acknowledge grants from Guangdong Basic and Applied Basic Research Foundation
774 (2021A1515110713) and Shenzhen Science and Technology Program



775 (JCYJ20210324104604012). The TROPOMI validation work was supported by BELSPO/ESA
776 through the ProDEX project TROVA-E2 (grant no. PEA 4000116692). TV acknowledges support
777 from BELSPO through BRAIN-BE 2.0 project LEGO-BEL-AQ (contract B2/191/P1/LEGO-
778 BEL-AQ). We thank Glenn Diskin for providing CO, CO₂, and CH₄ measurements. We thank Paul
779 Wennberg for H₂O₂ and HNO₃ measurements.

780

781 **Data Access**

782 The FTIR and MAXDOAS data used in this publication were partly obtained from the Network
783 for the Detection of Atmospheric Composition Change (NDACC) and are available through the
784 NDACC website www.ndacc.org. The spatial representation error is estimated based on publicly
785 available package, SpaTial Representation Error EstimaTor (STREET)
786 (<https://github.com/ahsouri/STREET>). DISCOVER-AQ and KORUS-AQ aircraft data can be
787 downloaded from <https://www-air.larc.nasa.gov/missions/discover-aq/discover-aq.html> and
788 <https://www-air.larc.nasa.gov/missions/korus-aq/>. TROPOMI NO₂ and HCHO data can be
789 downloaded from https://disc.gsfc.nasa.gov/datasets/S5P_L2_NO2_1/summary and
790 https://disc.gsfc.nasa.gov/datasets/S5P_L2_HCHO_1/summary. The box model results can be
791 obtained by contacting the corresponding author through ahsouri@cfa.harvard.edu.

792

793 **Author contributions**

794 AHS designed the research, analyzed the data, conducted the simulations, made all figures, and
795 wrote the paper. MSJ, SP, XL, and KC helped with conceptualization, fundraising, and analysis.
796 GMW helped with configuring the box model. AF, AW, WB, DRB, AJW, RCC, KM, and CC
797 measured various compounds during the air quality campaigns. JHC orchestrated all these
798 campaigns and contributed to the model interpretation. TV, SC, and GP provided paired MAX-
799 DOAS and TROPOMI tropospheric NO₂ observations. CV and BL provided paired FTIR and
800 TROPOMI HCHO observations. SC and LL provided paired integrated aircraft spirals and OMI
801 tropospheric NO₂ observations. LZ and SS provided the paired observations between the corrected
802 GEOS-Chem HCHO and OMI HCHO columns. All authors contributed to the discussion and
803 edited the paper.

804

805

806

807

808

809



810 References

- 811 Ahmadov, R., McKeen, S., Trainer, M., Banta, R., Brewer, A., Brown, S., Edwards, P.M., de
812 Gouw, J.A., Frost, G.J., Gilman, J., Helmig, D., Johnson, B., Karion, A., Koss, A.,
813 Langford, A., Lerner, B., Olson, J., Oltmans, S., Peischl, J., Pétron, G., Pichugina, Y.,
814 Roberts, J.M., Ryerson, T., Schnell, R., Senff, C., Sweeney, C., Thompson, C., Veres, P.R.,
815 Warneke, C., Wild, R., Williams, E.J., Yuan, B., Zamora, R., 2015. Understanding high
816 wintertime ozone pollution events in an oil- and natural gas-producing region of the western
817 US. *Atmospheric Chemistry and Physics* 15, 411–429. [https://doi.org/10.5194/acp-15-411-](https://doi.org/10.5194/acp-15-411-2015)
818 [2015](https://doi.org/10.5194/acp-15-411-2015)
- 819 Bela, M.M., Barth, M.C., Toon, O.B., Fried, A., Ziegler, C., Cummings, K.A., Li, Y., Pickering,
820 K.E., Homeyer, C.R., Morrison, H., Yang, Q., Mecikalski, R.M., Carey, L., Biggerstaff,
821 M.I., Betten, D.P., Alford, A.A., 2018. Effects of Scavenging, Entrainment, and Aqueous
822 Chemistry on Peroxides and Formaldehyde in Deep Convective Outflow Over the Central
823 and Southeast United States. *Journal of Geophysical Research: Atmospheres* 123, 7594–
824 7614. <https://doi.org/10.1029/2018JD028271>
- 825 Boeke, N.L., Marshall, J.D., Alvarez, S., Chance, K.V., Fried, A., Kurosu, T.P., Rappenglück, B.,
826 Richter, D., Walega, J., Weibring, P., Millet, D.B., 2011. Formaldehyde columns from the
827 Ozone Monitoring Instrument: Urban versus background levels and evaluation using aircraft
828 data and a global model. *Journal of Geophysical Research: Atmospheres* 116.
829 <https://doi.org/10.1029/2010JD014870>
- 830 Boersma, K.F., Eskes, H.J., Brinksma, E.J., 2004. Error analysis for tropospheric NO₂ retrieval
831 from space. *Journal of Geophysical Research: Atmospheres* 109.
832 <https://doi.org/10.1029/2003JD003962>
- 833 Boersma, K.F., Eskes, H.J., Richter, A., De Smedt, I., Lorente, A., Beirle, S., van Geffen,
834 J.H.G.M., Zara, M., Peters, E., Van Roozendaal, M., Wagner, T., Maasakkers, J.D., van der
835 A, R.J., Nightingale, J., De Rudder, A., Irie, H., Pinardi, G., Lambert, J.-C., Compernelle,
836 S.C., 2018. Improving algorithms and uncertainty estimates for satellite NO₂ retrievals:
837 results from the quality assurance for the essential climate variables (QA4ECV) project.
838 *Atmospheric Measurement Techniques* 11, 6651–6678. [https://doi.org/10.5194/amt-11-](https://doi.org/10.5194/amt-11-6651-2018)
839 [6651-2018](https://doi.org/10.5194/amt-11-6651-2018)
- 840 Boersma, K.F., Eskes, H.J., Veeffkind, J.P., Brinksma, E.J., van der A, R.J., Sneep, M., van den
841 Oord, G.H.J., Levelt, P.F., Stammes, P., Gleason, J.F., Bucsele, E.J., 2007. Near-real time
842 retrieval of tropospheric NO₂ from OMI. *Atmospheric Chemistry and Physics* 7, 2103–
843 2118. <https://doi.org/10.5194/acp-7-2103-2007>
- 844 Box, G.E.P., 1976. Science and Statistics. *Journal of the American Statistical Association* 71,
845 791–799. <https://doi.org/10.1080/01621459.1976.10480949>
- 846 Brune, W.H., Miller, D.O., Thames, A.B., Brosius, A.L., Barletta, B., Blake, D.R., Blake, N.J.,
847 Chen, G., Choi, Y., Crawford, J.H., Digangi, J.P., Diskin, G., Fried, A., Hall, S.R., Hanisco,
848 T.F., Huey, G.L., Hughes, S.C., Kim, M., Meinardi, S., Montzka, D.D., Pusede, S.E.,
849 Schroeder, J.R., Teng, A., Tanner, D.J., Ullmann, K., Walega, J., Weinheimer, A.,
850 Wisthaler, A., Wennberg, P.O., 2022. Observations of atmospheric oxidation and ozone
851 production in South Korea. *Atmospheric Environment* 269, 118854.
852 <https://doi.org/10.1016/j.atmosenv.2021.118854>
- 853 Chan, K.L., Wang, Z., Ding, A., Heue, K.-P., Shen, Y., Wang, J., Zhang, F., Shi, Y., Hao, N.,
854 Wenig, M., 2019. MAX-DOAS measurements of tropospheric NO₂ and HCHO in Nanjing



- 855 and a comparison to ozone monitoring instrument observations. *Atmospheric Chemistry and*
856 *Physics* 19, 10051–10071. <https://doi.org/10.5194/acp-19-10051-2019>
- 857 Chance, K., Palmer, P.I., Spurr, R.J.D., Martin, R.V., Kurosu, T.P., Jacob, D.J., 2000. Satellite
858 observations of formaldehyde over North America from GOME. *Geophysical Research*
859 *Letters* 27, 3461–3464. <https://doi.org/10.1029/2000GL011857>
- 860 Chance, K., Liu, X., Miller, C.C., Abad, G.G., Huang, G., Nowlan, C., Souri, A., Suleiman, R.,
861 Sun, K., Wang, H., Zhu, L., Zoogman, P., Al-Saadi, J., Antuña-Marrero, J.-C., Carr, J.,
862 Chatfield, R., Chin, M., Cohen, R., Edwards, D., Fishman, J., Flittner, D., Geddes, J.,
863 Grutter, M., Herman, J.R., Jacob, D.J., Janz, S., Joiner, J., Kim, J., Krotkov, N.A., Lefer, B.,
864 Martin, R.V., Mayol-Bracero, O.L., Naeger, A., Newchurch, M., Pfister, G.G., Pickering,
865 K., Pierce, R.B., Cárdenas, C.R., Saiz-Lopez, A., Simpson, W., Spinei, E., Spurr, R.J.D.,
866 Szykman, J.J., Torres, O., Wang, J., 2019. TEMPO Green Paper: Chemistry, physics, and
867 meteorology experiments with the Tropospheric Emissions: monitoring of pollution
868 instrument, in: *Sensors, Systems, and Next-Generation Satellites XXIII*. Presented at the
869 *Sensors, Systems, and Next-Generation Satellites XXIII*, SPIE, pp. 56–67.
870 <https://doi.org/10.1117/12.2534883>
- 871 Chance, K.V., Burrows, J.P., Perner, D., Schneider, W., 1997. Satellite measurements of
872 atmospheric ozone profiles, including tropospheric ozone, from ultraviolet/visible
873 measurements in the nadir geometry: a potential method to retrieve tropospheric ozone.
874 *Journal of Quantitative Spectroscopy and Radiative Transfer* 57, 467–476.
875 [https://doi.org/10.1016/S0022-4073\(96\)00157-4](https://doi.org/10.1016/S0022-4073(96)00157-4)
- 876 Chance, K.V., Burrows, J.P., Schneider, W., 1991. Retrieval and molecule sensitivity studies for
877 the global ozone monitoring experiment and the scanning imaging absorption spectrometer
878 for atmospheric cartography, in: *Remote Sensing of Atmospheric Chemistry*. Presented at
879 the *Remote Sensing of Atmospheric Chemistry*, SPIE, pp. 151–165.
880 <https://doi.org/10.1117/12.46657>
- 881 Choi, S., Lamsal, L.N., Follette-Cook, M., Joiner, J., Krotkov, N.A., Swartz, W.H., Pickering,
882 K.E., Loughner, C.P., Appel, W., Pfister, G., Saide, P.E., Cohen, R.C., Weinheimer, A.J.,
883 Herman, J.R., 2020. Assessment of NO₂ observations during DISCOVER-AQ and KORUS-
884 AQ field campaigns. *Atmospheric Measurement Techniques* 13, 2523–2546.
885 <https://doi.org/10.5194/amt-13-2523-2020>
- 886 Choi, Y., Kim, H., Tong, D., Lee, P., 2012b. Summertime weekly cycles of observed and
887 modeled NO_x and O₃ concentrations as a function of satellite-derived ozone production
888 sensitivity and land use types over the Continental United States. *Atmospheric Chemistry*
889 *and Physics* 12, 6291–6307. <https://doi.org/10.5194/acp-12-6291-2012>
- 890 Choi, Y., Souri, A.H., 2015a. Seasonal behavior and long-term trends of tropospheric ozone, its
891 precursors and chemical conditions over Iran: A view from space. *Atmospheric*
892 *Environment* 106, 232–240. <https://doi.org/10.1016/j.atmosenv.2015.02.012>
- 893 Choi, Y., Souri, A.H., 2015b. Chemical condition and surface ozone in large cities of Texas
894 during the last decade: Observational evidence from OMI, CAMS, and model analysis.
895 *Remote Sensing of Environment* 168, 90–101. <https://doi.org/10.1016/j.rse.2015.06.026>
- 896 Crawford, J.H., Ahn, J.-Y., Al-Saadi, J., Chang, L., Emmons, L.K., Kim, J., Lee, G., Park, J.-H.,
897 Park, R.J., Woo, J.H., Song, C.-K., Hong, J.-H., Hong, Y.-D., Lefer, B.L., Lee, M., Lee, T.,
898 Kim, S., Min, K.-E., Yum, S.S., Shin, H.J., Kim, Y.-W., Choi, J.-S., Park, J.-S., Szykman,
899 J.J., Long, R.W., Jordan, C.E., Simpson, I.J., Fried, A., Dibb, J.E., Cho, S., Kim, Y.P., 2021.



- 900 The Korea–United States Air Quality (KORUS-AQ) field study. *Elementa: Science of the*
901 *Anthropocene* 9, 00163. <https://doi.org/10.1525/elementa.2020.00163>
- 902 de Gouw, J.A., Gilman, J.B., Kim, S.-W., Alvarez, S.L., Dusanter, S., Graus, M., Griffith, S.M.,
903 Isaacman-VanWertz, G., Kuster, W.C., Lefer, B.L., Lerner, B.M., McDonald, B.C.,
904 Rappenglück, B., Roberts, J.M., Stevens, P.S., Stutz, J., Thalman, R., Veres, P.R.,
905 Volkamer, R., Warneke, C., Washenfelder, R.A., Young, C.J., 2018. Chemistry of Volatile
906 Organic Compounds in the Los Angeles Basin: Formation of Oxygenated Compounds and
907 Determination of Emission Ratios. *Journal of Geophysical Research: Atmospheres* 123,
908 2298–2319. <https://doi.org/10.1002/2017JD027976>
- 909 De Smedt, I., Müller, J.-F., Stavrou, T., van der A, R., Eskes, H., Van Roozendaal, M., 2008.
910 Twelve years of global observations of formaldehyde in the troposphere using GOME and
911 SCIAMACHY sensors. *Atmospheric Chemistry and Physics* 8, 4947–4963.
912 <https://doi.org/10.5194/acp-8-4947-2008>
- 913 De Smedt, I., Pinardi, G., Vigouroux, C., Compernelle, S., Bais, A., Benavent, N., Boersma, F.,
914 Chan, K.-L., Donner, S., Eichmann, K.-U., Hedelt, P., Hendrick, F., Irie, H., Kumar, V.,
915 Lambert, J.-C., Langerock, B., Lerot, C., Liu, C., Loyola, D., Peters, A., Richter, A., Rivera
916 Cárdenas, C., Romahn, F., Ryan, R.G., Sinha, V., Theys, N., Vlietinck, J., Wagner, T.,
917 Wang, T., Yu, H., Van Roozendaal, M., 2021. Comparative assessment of TROPOMI and
918 OMI formaldehyde observations and validation against MAX-DOAS network column
919 measurements. *Atmospheric Chemistry and Physics* 21, 12561–12593.
920 <https://doi.org/10.5194/acp-21-12561-2021>
- 921 De Smedt, I., Stavrou, T., Hendrick, F., Danckaert, T., Vlemmix, T., Pinardi, G., Theys, N.,
922 Lerot, C., Gielen, C., Vigouroux, C., Hermans, C., Fayt, C., Veefkind, P., Müller, J.-F., Van
923 Roozendaal, M., 2015. Diurnal, seasonal and long-term variations of global formaldehyde
924 columns inferred from combined OMI and GOME-2 observations. *Atmospheric Chemistry*
925 *and Physics* 15, 12519–12545. <https://doi.org/10.5194/acp-15-12519-2015>
- 926 De Smedt, I., Stavrou, T., Müller, J.-F., van der A, R.J., Van Roozendaal, M., 2010. Trend
927 detection in satellite observations of formaldehyde tropospheric columns. *Geophysical*
928 *Research Letters* 37. <https://doi.org/10.1029/2010GL044245>
- 929 De Smedt, I., Theys, N., Yu, H., Danckaert, T., Lerot, C., Compernelle, S., Van Roozendaal, M.,
930 Richter, A., Hilboll, A., Peters, E., Pedergnana, M., Loyola, D., Beirle, S., Wagner, T.,
931 Eskes, H., van Geffen, J., Boersma, K.F., Veefkind, P., 2018. Algorithm theoretical baseline
932 for formaldehyde retrievals from S5P TROPOMI and from the QA4ECV project.
933 *Atmospheric Measurement Techniques* 11, 2395–2426. [https://doi.org/10.5194/amt-11-](https://doi.org/10.5194/amt-11-2395-2018)
934 [2395-2018](https://doi.org/10.5194/amt-11-2395-2018)
- 935 Diao, L., Choi, Y., Czader, B., Li, X., Pan, S., Roy, A., Sour, A.H., Estes, M., Jeon, W., 2016.
936 Discrepancies between modeled and observed nocturnal isoprene in an urban environment
937 and the possible causes: A case study in Houston. *Atmospheric Research* 181, 257–264.
938 <https://doi.org/10.1016/j.atmosres.2016.07.009>
- 939 Duncan, B.N., Yoshida, Y., Olson, J.R., Sillman, S., Martin, R.V., Lamsal, L., Hu, Y., Pickering,
940 K.E., Retscher, C., Allen, D.J., Crawford, J.H., 2010. Application of OMI observations to a
941 space-based indicator of NO_x and VOC controls on surface ozone formation. *Atmospheric*
942 *Environment* 44, 2213–2223. <https://doi.org/10.1016/j.atmosenv.2010.03.010>
- 943 Fried, A., Walega, J., Weibring, P., Richter, D., Simpson, I.J., Blake, D.R., Blake, N.J., Meinardi,
944 S., Barletta, B., Hughes, S.C., Crawford, J.H., Diskin, G., Barrick, J., Hair, J., Fenn, M.,
945 Wisthaler, A., Mikoviny, T., Woo, J.-H., Park, M., Kim, Jinseok, Min, K.-E., Jeong, S.,



- 946 Wennberg, P.O., Kim, M.J., Crounse, J.D., Teng, A.P., Bennett, R., Yang-Martin, M.,
947 Shook, M.A., Huey, G., Tanner, D., Knote, C., Kim, JongHo, Park, R., Brune, W., 2020.
948 Airborne formaldehyde and volatile organic compound measurements over the Daesan
949 petrochemical complex on Korea's northwest coast during the Korea-United States Air
950 Quality study: Estimation of emission fluxes and effects on air quality. *Elementa: Science of*
951 *the Anthropocene* 8, 121. <https://doi.org/10.1525/elementa.2020.121>
- 952 González Abad, G., Liu, X., Chance, K., Wang, H., Kurosu, T.P., Suleiman, R., 2015. Updated
953 Smithsonian Astrophysical Observatory Ozone Monitoring Instrument (SAO OMI)
954 formaldehyde retrieval. *Atmospheric Measurement Techniques* 8, 19–32.
955 <https://doi.org/10.5194/amt-8-19-2015>
- 956 Gonzalez Abad, G., Souri, A.H., Bak, J., Chance, K., Flynn, L.E., Krotkov, N.A., Lamsal, L., Li,
957 C., Liu, X., Miller, C.C., Nowlan, C.R., Suleiman, R., Wang, H., 2019. Five decades
958 observing Earth's atmospheric trace gases using ultraviolet and visible backscatter solar
959 radiation from space. *Journal of Quantitative Spectroscopy and Radiative Transfer* 238,
960 106478. <https://doi.org/10.1016/j.jqsrt.2019.04.030>
- 961 Janjić, T., Bormann, N., Bocquet, M., Carton, J.A., Cohn, S.E., Dance, S.L., Losa, S.N., Nichols,
962 N.K., Potthast, R., Waller, J.A., Weston, P., 2018. On the representation error in data
963 assimilation. *Quarterly Journal of the Royal Meteorological Society* 144, 1257–1278.
964 <https://doi.org/10.1002/qj.3130>
- 965 Jeon, W., Choi, Y., Souri, A.H., Roy, A., Diao, L., Pan, S., Lee, H.W., Lee, S.-H., 2018.
966 Identification of chemical fingerprints in long-range transport of burning induced upper
967 tropospheric ozone from Colorado to the North Atlantic Ocean. *Science of The Total*
968 *Environment* 613–614, 820–828. <https://doi.org/10.1016/j.scitotenv.2017.09.177>
- 969 Jin, X., Fiore, A.M., Murray, L.T., Valin, L.C., Lamsal, L.N., Duncan, B., Folkert Boersma, K.,
970 De Smedt, I., Abad, G.G., Chance, K., Tonnesen, G.S., 2017. Evaluating a Space-Based
971 Indicator of Surface Ozone-NO_x-VOC Sensitivity Over Midlatitude Source Regions and
972 Application to Decadal Trends. *Journal of Geophysical Research: Atmospheres* 122,
973 10,439-10,461. <https://doi.org/10.1002/2017JD026720>
- 974 Jin, X., Holloway, T., 2015. Spatial and temporal variability of ozone sensitivity over China
975 observed from the Ozone Monitoring Instrument. *Journal of Geophysical Research:*
976 *Atmospheres* 120, 7229–7246. <https://doi.org/10.1002/2015JD023250>
- 977 Kleinman, L.I., Daum, P.H., Lee, Y.-N., Nunnermacker, L.J., Springston, S.R., Weinstein-Lloyd,
978 J., Rudolph, J., 2001. Sensitivity of ozone production rate to ozone precursors. *Geophysical*
979 *Research Letters* 28, 2903–2906. <https://doi.org/10.1029/2000GL012597>
- 980 Laughner, J.L., Zhu, Q., Cohen, R.C., 2019. Evaluation of version 3.0B of the BEHR OMI NO₂
981 product. *Atmospheric Measurement Techniques* 12, 129–146. [https://doi.org/10.5194/amt-](https://doi.org/10.5194/amt-12-129-2019)
982 [12-129-2019](https://doi.org/10.5194/amt-12-129-2019)
- 983 Lee, H.-J., Chang, L.-S., Jaffe, D.A., Bak, J., Liu, X., Abad, G.G., Jo, H.-Y., Jo, Y.-J., Lee, J.-B.,
984 Yang, G.-H., Kim, J.-M., Kim, C.-H., 2022. Satellite-Based Diagnosis and Numerical
985 Verification of Ozone Formation Regimes over Nine Megacities in East Asia. *Remote*
986 *Sensing* 14, 1285. <https://doi.org/10.3390/rs14051285>
- 987 Lee, Y., Huey, L.G., Wang, Y., Qu, H., Zhang, R., Ji, Y., Tanner, D.J., Wang, X., Tang, J., Song,
988 W., Hu, W., Zhang, Y., 2021. Photochemistry of Volatile Organic Compounds in the
989 Yellow River Delta, China: Formation of O₃ and Peroxyacyl Nitrates. *Journal of*
990 *Geophysical Research: Atmospheres* 126, e2021JD035296.
991 <https://doi.org/10.1029/2021JD035296>



- 992 Martin, R.V., Chance, K., Jacob, D.J., Kurosu, T.P., Spurr, R.J.D., Bucselá, E., Gleason, J.F.,
993 Palmer, P.I., Bey, I., Fiore, A.M., Li, Q., Yantosca, R.M., Koelemeijer, R.B.A., 2002. An
994 improved retrieval of tropospheric nitrogen dioxide from GOME. *Journal of Geophysical*
995 *Research: Atmospheres* 107, ACH 9-1-ACH 9-21. <https://doi.org/10.1029/2001JD001027>
996 Martin, R.V., Fiore, A.M., Van Donkelaar, A., 2004. Space-based diagnosis of surface ozone
997 sensitivity to anthropogenic emissions. *Geophysical Research Letters* 31.
998 <https://doi.org/10.1029/2004GL019416>
999 Matheron, G., 1963. Principles of geostatistics. *Economic Geology* 58, 1246–1266.
1000 <https://doi.org/10.2113/gsecongeo.58.8.1246>
1001 Newland, M.J., Bryant, D.J., Dunmore, R.E., Bannan, T.J., Acton, W.J.F., Langford, B.,
1002 Hopkins, J.R., Squires, F.A., Dixon, W., Drysdale, W.S., Ivatt, P.D., Evans, M.J., Edwards,
1003 P.M., Whalley, L.K., Heard, D.E., Slater, E.J., Woodward-Massey, R., Ye, C., Mehra, A.,
1004 Worrall, S.D., Bacak, A., Coe, H., Percival, C.J., Hewitt, C.N., Lee, J.D., Cui, T., Surratt,
1005 J.D., Wang, X., Lewis, A.C., Rickard, A.R., Hamilton, J.F., 2021. Low-NO atmospheric
1006 oxidation pathways in a polluted megacity. *Atmospheric Chemistry and Physics* 21, 1613–
1007 1625. <https://doi.org/10.5194/acp-21-1613-2021>
1008 Nunnermacker, L.J., Weinstein-Lloyd, J., Kleinman, L., Daum, P.H., Lee, Y.N., Springston,
1009 S.R., Klotz, P., Newman, L., Neuroth, G., Hyde, P., 2004. Ground-based and aircraft
1010 measurements of trace gases in Phoenix, Arizona (1998). *Atmospheric Environment* 38,
1011 4941–4956. <https://doi.org/10.1016/j.atmosenv.2004.04.033>
1012 Pan, S., Choi, Y., Roy, A., Li, X., Jeon, W., Souri, A.H., 2015. Modeling the uncertainty of
1013 several VOC and its impact on simulated VOC and ozone in Houston, Texas. *Atmospheric*
1014 *Environment* 120, 404–416. <https://doi.org/10.1016/j.atmosenv.2015.09.029>
1015 Rappenglück, B., Ackermann, L., Alvarez, S., Golovko, J., Buhr, M., Field, R.A., Soltis, J.,
1016 Montague, D.C., Hauze, B., Adamson, S., Risch, D., Wilkerson, G., Bush, D., Stoeckenius,
1017 T., Keslar, C., 2014. Strong wintertime ozone events in the Upper Green River basin,
1018 Wyoming. *Atmospheric Chemistry and Physics* 14, 4909–4934. [https://doi.org/10.5194/acp-](https://doi.org/10.5194/acp-14-4909-2014)
1019 [14-4909-2014](https://doi.org/10.5194/acp-14-4909-2014)
1020 Ren, B., Xie, P., Xu, J., Li, A., Qin, M., Hu, R., Zhang, T., Fan, G., Tian, X., Zhu, W., Hu, Z.,
1021 Huang, Y., Li, X., Meng, F., Zhang, G., Tong, J., Ren, H., Zheng, J., Zhang, Z., Lv, Y.,
1022 2022. Vertical characteristics of NO₂ and HCHO, and the ozone formation regimes in
1023 Hefei, China. *Science of The Total Environment* 823, 153425.
1024 <https://doi.org/10.1016/j.scitotenv.2022.153425>
1025 Schroeder, J.R., Crawford, J.H., Fried, A., Walega, J., Weinheimer, A., Wisthaler, A., Müller,
1026 M., Mikoviny, T., Chen, G., Shook, M., Blake, D.R., Tonnesen, G.S., 2017. New insights
1027 into the column CH₂O/NO₂ ratio as an indicator of near-surface ozone sensitivity. *Journal*
1028 *of Geophysical Research: Atmospheres* 122, 8885–8907.
1029 <https://doi.org/10.1002/2017JD026781>
1030 Schroeder, J.R., Crawford, J.H., Ahn, J.-Y., Chang, L., Fried, A., Walega, J., Weinheimer, A.,
1031 Montzka, D.D., Hall, S.R., Ullmann, K., Wisthaler, A., Mikoviny, T., Chen, G., Blake,
1032 D.R., Blake, N.J., Hughes, S.C., Meinardi, S., Diskin, G., Digangi, J.P., Choi, Y., Pusede,
1033 S.E., Huey, G.L., Tanner, D.J., Kim, M., Wennberg, P., 2020. Observation-based modeling
1034 of ozone chemistry in the Seoul metropolitan area during the Korea-United States Air
1035 Quality Study (KORUS-AQ). *Elementa: Science of the Anthropocene* 8, 3.
1036 <https://doi.org/10.1525/elementa.400>
1037



- 1038 Schwaerzel, M., Emde, C., Brunner, D., Morales, R., Wagner, T., Berne, A., Buchmann, B.,
1039 Kuhlmann, G., 2020. Three-dimensional radiative transfer effects on airborne and ground-
1040 based trace gas remote sensing. *Atmospheric Measurement Techniques* 13, 4277–4293.
1041 <https://doi.org/10.5194/amt-13-4277-2020>
- 1042 Seinfeld, J. H. and Pandis, S. N., 2006: *Atmospheric Chemistry and Physics: From Air Pollution to*
1043 *Climate Change*, 2nd Edn., Wiley-Interscience, Hoboken, N.J., ISBN: 978-1-118-94740-
1044 1.
- 1045 Sillman, S., He, D., 2002. Some theoretical results concerning O₃-NO_x-VOC chemistry and
1046 NO_x-VOC indicators. *Journal of Geophysical Research: Atmospheres* 107, ACH 26-1-ACH
1047 26-15. <https://doi.org/10.1029/2001JD001123>
- 1048 Sillman, S., Logan, J.A., Wofsy, S.C., 1990. The sensitivity of ozone to nitrogen oxides and
1049 hydrocarbons in regional ozone episodes. *Journal of Geophysical Research: Atmospheres*
1050 95, 1837–1851. <https://doi.org/10.1029/JD095iD02p01837>
- 1051 Souri, A.H., Chance, K., Bak, J., Nowlan, C.R., González Abad, G., Jung, Y., Wong, D.C., Mao,
1052 J., Liu, X., 2021. Unraveling pathways of elevated ozone induced by the 2020 lockdown in
1053 Europe by an observationally constrained regional model using TROPOMI. *Atmospheric*
1054 *Chemistry and Physics* 21, 18227–18245. <https://doi.org/10.5194/acp-21-18227-2021>
- 1055 Souri, A.H., Chance, K., Sun, K., Liu, X., Johnson, M.S., 2022. Dealing with spatial
1056 heterogeneity in pointwise-to-gridded- data comparisons. *Atmospheric Measurement*
1057 *Techniques* 15, 41–59. <https://doi.org/10.5194/amt-15-41-2022>
- 1058 Souri, A.H., Nowlan, C.R., Wolfe, G.M., Lamsal, L.N., Chan Miller, C.E., Abad, G.G., Janz,
1059 S.J., Fried, A., Blake, D.R., Weinheimer, A.J., Diskin, G.S., Liu, X., Chance, K., 2020.
1060 Revisiting the effectiveness of HCHO/NO₂ ratios for inferring ozone sensitivity to its
1061 precursors using high resolution airborne remote sensing observations in a high ozone
1062 episode during the KORUS-AQ campaign. *Atmospheric Environment* 224, 117341.
1063 <https://doi.org/10.1016/j.atmosenv.2020.117341>
- 1064 Tang, W., Edwards, D.P., Emmons, L.K., Worden, H.M., Judd, L.M., Lamsal, L.N., Al-Saadi,
1065 J.A., Janz, S.J., Crawford, J.H., Deeter, M.N., Pfister, G., Buchholz, R.R., Gaubert, B.,
1066 Nowlan, C.R., 2021. Assessing sub-grid variability within satellite pixels over urban regions
1067 using airborne mapping spectrometer measurements. *Atmospheric Measurement Techniques*
1068 14, 4639–4655. <https://doi.org/10.5194/amt-14-4639-2021>
- 1069 Thornton, J.A., Wooldridge, P.J., Cohen, R.C., Martinez, M., Harder, H., Brune, W.H., Williams,
1070 E.J., Roberts, J.M., Fehsenfeld, F.C., Hall, S.R., Shetter, R.E., Wert, B.P., Fried, A., 2002.
1071 Ozone production rates as a function of NO_x abundances and HO_x production rates in the
1072 Nashville urban plume. *Journal of Geophysical Research: Atmospheres* 107, ACH 7-1-ACH
1073 7-17. <https://doi.org/10.1029/2001JD000932>
- 1074 Tonnesen, G.S., Dennis, R.L., 2000a. Analysis of radical propagation efficiency to assess ozone
1075 sensitivity to hydrocarbons and NO_x : 1. Local indicators of instantaneous odd oxygen
1076 production sensitivity. *Journal of Geophysical Research: Atmospheres* 105, 9213–9225.
1077 <https://doi.org/10.1029/1999JD900371>
- 1078 Tonnesen, G.S., Dennis, R.L., 2000b. Analysis of radical propagation efficiency to assess ozone
1079 sensitivity to hydrocarbons and NO_x : 2. Long-lived species as indicators of ozone
1080 concentration sensitivity. *Journal of Geophysical Research: Atmospheres* 105, 9227–9241.
1081 <https://doi.org/10.1029/1999JD900372>



- 1082 Valin, L.C., Russell, A.R., Hudman, R.C., Cohen, R.C., 2011. Effects of model resolution on the
1083 interpretation of satellite NO₂ observations. *Atmospheric Chemistry and Physics* 11,
1084 11647–11655. <https://doi.org/10.5194/acp-11-11647-2011>
- 1085 van Geffen, J., Eskes, H., Compornolle, S., Pinardi, G., Verhoelst, T., Lambert, J.-C., Sneep, M.,
1086 ter Linden, M., Ludewig, A., Boersma, K.F., Veeffkind, J.P., 2022. Sentinel-5P TROPOMI
1087 NO₂ retrieval: impact of version v2.2 improvements and comparisons with OMI and
1088 ground-based data. *Atmospheric Measurement Techniques* 15, 2037–2060.
1089 <https://doi.org/10.5194/amt-15-2037-2022>
- 1090 Verhoelst, T., Compornolle, S., Pinardi, G., Lambert, J.-C., Eskes, H.J., Eichmann, K.-U.,
1091 Fjæraa, A.M., Granville, J., Niemeijer, S., Cede, A., Tiefengraber, M., Hendrick, F.,
1092 Pazmiño, A., Bais, A., Bazureau, A., Boersma, K.F., Bogner, K., Dehn, A., Donner, S.,
1093 Elokhov, A., Gebetsberger, M., Goutail, F., Grutter de la Mora, M., Gruzdev, A., Gratsea,
1094 M., Hansen, G.H., Irie, H., Jepsen, N., Kanaya, Y., Karagkiozidis, D., Kivi, R., Kreher, K.,
1095 Levelt, P.F., Liu, C., Müller, M., Navarro Comas, M., Piters, A.J.M., Pommereau, J.-P.,
1096 Portafaix, T., Prados-Roman, C., Puertedura, O., Querel, R., Remmers, J., Richter, A.,
1097 Rimmer, J., Rivera Cárdenas, C., Saavedra de Miguel, L., Sinyakov, V.P., Stremme, W.,
1098 Strong, K., Van Roozendaal, M., Veeffkind, J.P., Wagner, T., Wittrock, F., Yela González,
1099 M., Zehner, C., 2021. Ground-based validation of the Copernicus Sentinel-5P TROPOMI
1100 NO₂ measurements with the NDACC ZSL-DOAS, MAX-DOAS and Pandonia global
1101 networks. *Atmospheric Measurement Techniques* 14, 481–510. <https://doi.org/10.5194/amt-14-481-2021>
- 1102
- 1103 Vigouroux, C., Langerock, B., Bauer Aquino, C. A., Blumenstock, T., Cheng, Z., De Mazière,
1104 M., De Smedt, I., Grutter, M., Hannigan, J. W., Jones, N., Kivi, R., Loyola, D., Lutsch, E.,
1105 Mahieu, E., Makarova, M., Metzger, J.-M., Morino, I., Murata, I., Nagahama, T., Notholt,
1106 J., Ortega, I., Palm, M., Pinardi, G., Röhling, A., Smale, D., Stremme, W., Strong, K.,
1107 Sussmann, R., Té, Y., van Roozendaal, M., Wang, P., and Winkler, H.: TROPOMI–
1108 Sentinel-5 Precursor formaldehyde validation using an extensive network of ground-based
1109 Fourier-transform infrared stations, *Atmos. Meas. Tech.*, 13, 3751–3767,
1110 <https://doi.org/10.5194/amt-13-3751-2020>, 2020.
- 1111 Wells, K.C., Millet, D.B., Payne, V.H., Deventer, M.J., Bates, K.H., de Gouw, J.A., Graus, M.,
1112 Warneke, C., Wisthaler, A., Fuentes, J.D., 2020. Satellite isoprene retrievals constrain
1113 emissions and atmospheric oxidation. *Nature* 585, 225–233. <https://doi.org/10.1038/s41586-020-2664-3>
- 1114
- 1115 Wolfe, G. M., Kaiser, J., Hanisco, T.F., Keutsch, F.N., de Gouw, J.A., Gilman, J.B., Graus, M.,
1116 Hatch, C.D., Holloway, J., Horowitz, L.W., Lee, B.H., Lerner, B.M., Lopez-Hilifiker, F.,
1117 Mao, J., Marvin, M.R., Peischl, J., Pollack, I.B., Roberts, J.M., Ryerson, T.B., Thornton,
1118 J.A., Veres, P.R., Warneke, C., 2016. Formaldehyde production from isoprene oxidation
1119 across NO_x regimes. *Atmospheric Chemistry and Physics* 16, 2597–2610.
1120 <https://doi.org/10.5194/acp-16-2597-2016>
- 1121 Wolfe, Glenn M., Marvin, M.R., Roberts, S.J., Travis, K.R., Liao, J., 2016. The Framework for
1122 0-D Atmospheric Modeling (F0AM) v3.1. *Geoscientific Model Development* 9, 3309–3319.
1123 <https://doi.org/10.5194/gmd-9-3309-2016>
- 1124 Xu, W., Zhang, G., Wang, Y., Tong, S., Zhang, W., Ma, Z., Lin, W., Kuang, Y., Yin, L., Xu, X.,
1125 2021. Aerosol Promotes Peroxyacetyl Nitrate Formation During Winter in the North China
1126 Plain. *Environ. Sci. Technol.* 55, 3568–3581. <https://doi.org/10.1021/acs.est.0c08157>



- 1127 Yang, K., Carn, S.A., Ge, C., Wang, J., Dickerson, R.R., 2014. Advancing measurements of
1128 tropospheric NO₂ from space: New algorithm and first global results from OMPS.
1129 Geophysical Research Letters 41, 4777–4786. <https://doi.org/10.1002/2014GL060136>
1130 Zhang, K., Duan, Y., Huo, J., Huang, L., Wang, Yangjun, Fu, Q., Wang, Yuhang, Li, L., 2021.
1131 Formation mechanism of HCHO pollution in the suburban Yangtze River Delta region,
1132 China: A box model study and policy implementations. Atmospheric Environment 267,
1133 118755. <https://doi.org/10.1016/j.atmosenv.2021.118755>
1134 Zhu, L., González Abad, G., Nowlan, C.R., Chan Miller, C., Chance, K., Apel, E.C., DiGangi,
1135 J.P., Fried, A., Hanisco, T.F., Hornbrook, R.S., Hu, L., Kaiser, J., Keutsch, F.N., Permar,
1136 W., St. Clair, J.M., Wolfe, G.M., 2020. Validation of satellite formaldehyde (HCHO)
1137 retrievals using observations from 12 aircraft campaigns. Atmospheric Chemistry and
1138 Physics 20, 12329–12345. <https://doi.org/10.5194/acp-20-12329-2020>
1139 Zhu, L., Jacob, D.J., Kim, P.S., Fisher, J.A., Yu, K., Travis, K.R., Mickley, L.J., Yantosca, R.M.,
1140 Sulprizio, M.P., De Smedt, I., González Abad, G., Chance, K., Li, C., Ferrare, R., Fried, A.,
1141 Hair, J.W., Hanisco, T.F., Richter, D., Jo Scarino, A., Walega, J., Weibring, P., Wolfe,
1142 G.M., 2016. Observing atmospheric formaldehyde (HCHO) from space: validation and
1143 intercomparison of six retrievals from four satellites (OMI, GOME2A, GOME2B, OMPS)
1144 with SEAC⁴RS aircraft observations over the southeast US. Atmospheric Chemistry and
1145 Physics 16, 13477–13490. <https://doi.org/10.5194/acp-16-13477-2016>
1146 Zhu, L., Jacob, D.J., Mickley, L.J., Marais, E.A., Cohan, D.S., Yoshida, Y., Duncan, B.N., Abad,
1147 G.G., Chance, K.V., 2014. Anthropogenic emissions of highly reactive volatile organic
1148 compounds in eastern Texas inferred from oversampling of satellite (OMI) measurements of
1149 HCHO columns. Environ. Res. Lett. 9, 114004. [https://doi.org/10.1088/1748-](https://doi.org/10.1088/1748-9326/9/11/114004)
1150 [9326/9/11/114004](https://doi.org/10.1088/1748-9326/9/11/114004)
1151



1152
 1153
 1154

Table 1. The box model configurations and inputs.

Temporal resolution of samples	10-15 sec
Time steps	1 hour
Number of solar cycles	5
Dilution constant	1/86400 -1/43200 (s ⁻¹)
Meteorological Inputs	Pressure, Temperature, and Relative Humidity
Photolysis frequencies estimates	LUT based on the NCAR TUV model calculations
Photolysis frequencies constraints (campaign#‡)	Measured jNO ₂ (1-4) and jO ¹ D (4)
Compounds (Instrument#†, campaign#‡) used for constraining the box model	H ₂ (1, 4)§, CO (4, 1-4), NO _x (2, 1-4), O ₃ (2, 1-4), SO ₂ (6, 4), CH ₄ (4, 1-4), HNO ₃ (10, 1-4), Isoprene (9, 1-4), Monoterpenes (9, 1-4), Acetone (9, 1-4), Ethylene (1, 4), Ethane (1, 4), Methanol (9, 1-4), Propane (1, 4), Benzene (1 or 9, 2-4), Xylene (1 or 9, 1 and 4), Toluene (1 or 9, 1-4), Glyoxal (8, 4), Acetaldehyde (9, 1-4), Methyl vinyl ketone (9, 1-4), Methyl Ethyl Ketone (9, 2-4), Propene (1 or 9, 2 and 4), Acetic acid (9, 2-4), Glycolaldehyde (5, 4), H ₂ O ₂ (5, 4)
Unconstrained compounds (Instrument#†, campaign#‡) used for validation	HO ₂ (3, 4), OH (3, 4), NO (2, 1-4), NO ₂ (2, 1-4), PAN (10, 1-4), HCHO (7, 1-4)
Chemical Mechanism	CB06

1155
 1156
 1157
 1158
 1159
 1160
 1161
 1162
 1163
 1164
 1165
 1166
 1167
 1168

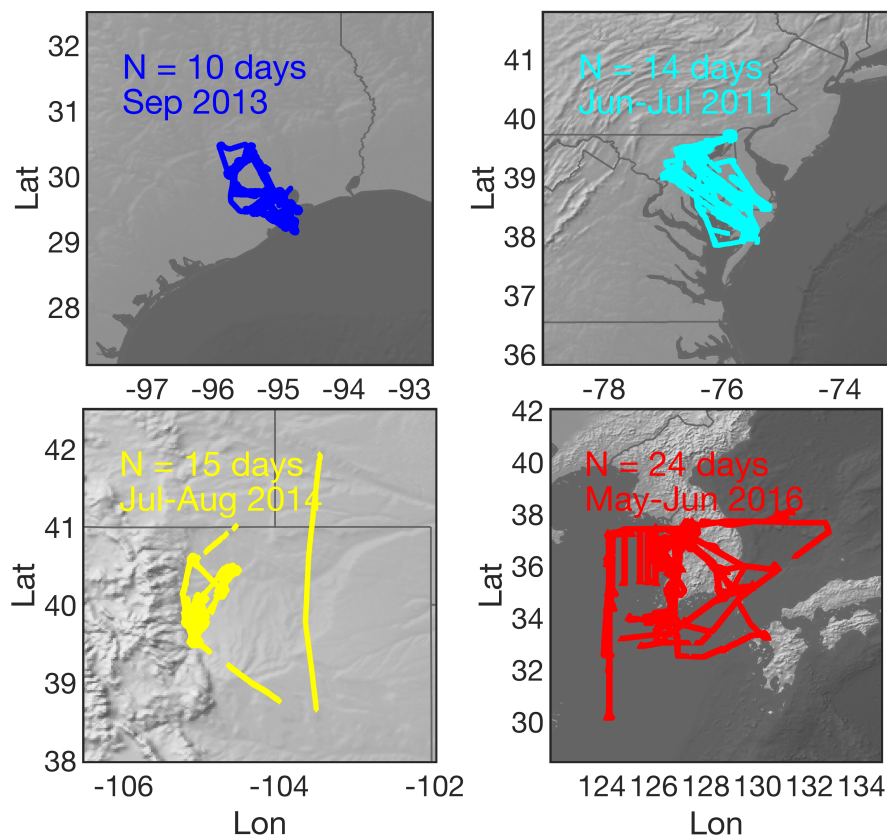
† (1) UC Irvine's Whole Air Sampler (WAS), (2) NCAR 4-Channel Chemiluminescence, (3) Penn State's Airborne Tropospheric Hydrogen Oxides Sensor (ATHOS), (4) NASA Langley's DACOM tunable diode laser spectrometer, (5) Caltech's single mass analyzer, (6) Georgia Tech's ionization mass spectrometer, (7) The University of Colorado at Boulder's the Compact Atmospheric Multi-species Spectrometer (CAMS), (8) Korean Airborne Cavity Enhances Spectrometer, (9) University of Innsbruck's PTR-TOF-MS instrument, and (10) University of California, Berkeley's TD-LIF.

‡ (1) DISCOVER-Baltimore-Washington, (2) DISCOVER-Texas-Houston, (3) DISCOVER-Colorado, and (4) KORUS-AQ

§ In the absence of measurements, a default value of 550 ppbv is specified.

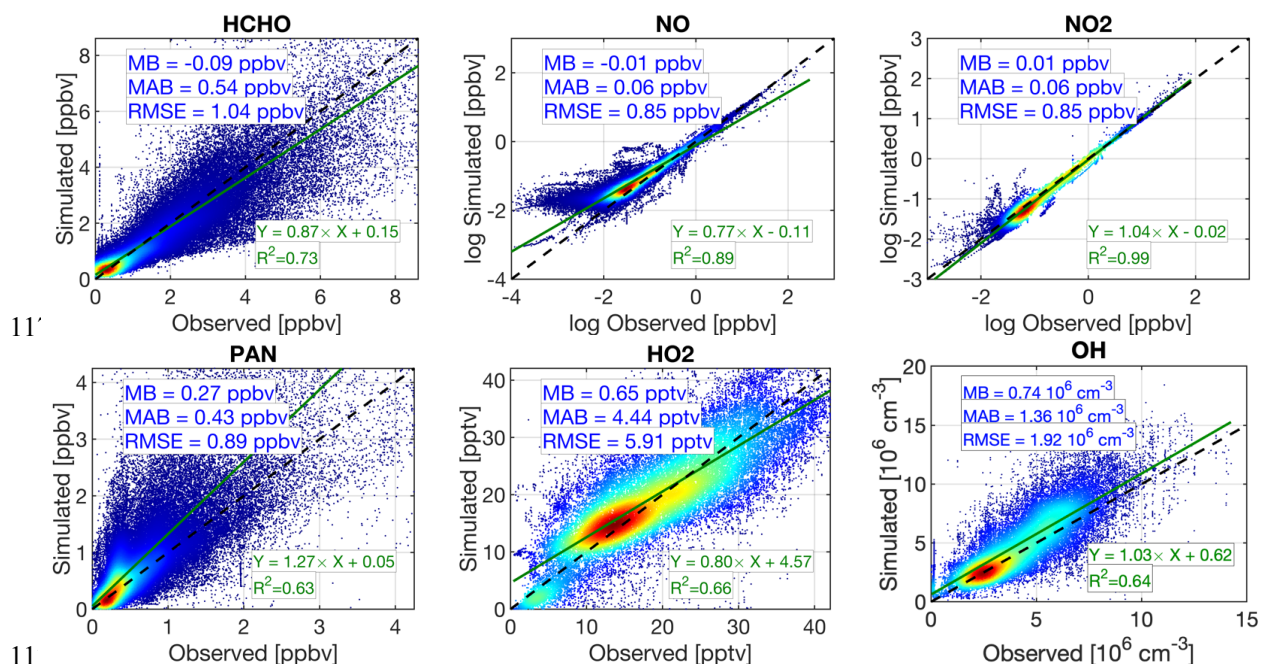


1169



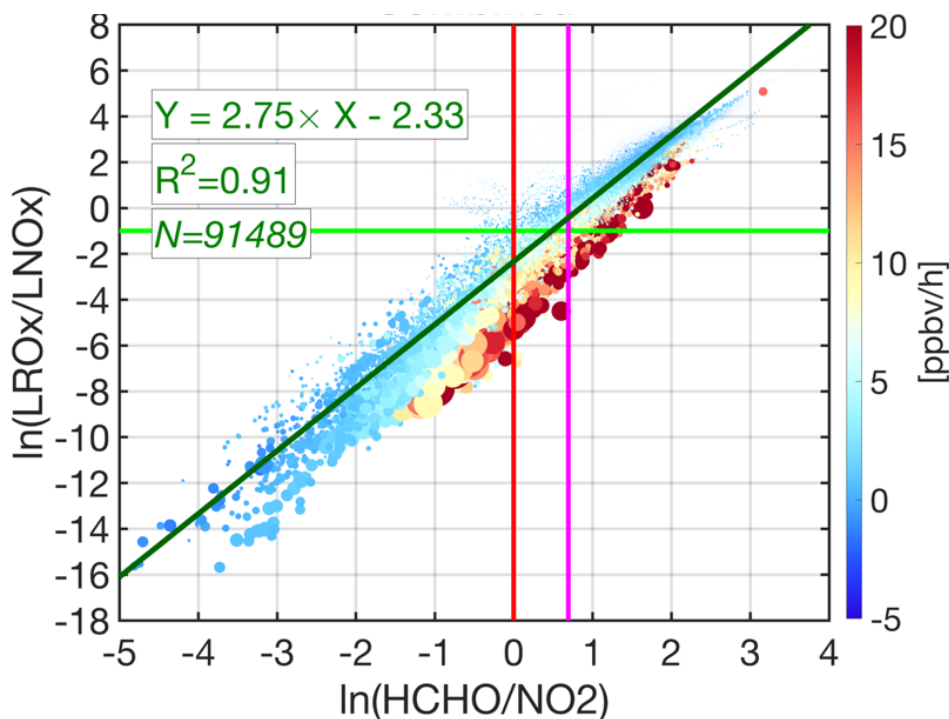
1170
1171
1172
1173
1174
1175
1176

Figure 1. The spatial distributions of aircraft measurements collected during NASA's a) DISCOVER-AQ Houston-Texas, b) DISCOVER-AQ Baltimore-Washington, c) DISCOVER-AQ Colorado, and d) KORUS-AQ. The duration of each campaign is based on how long the aircraft was in the air.



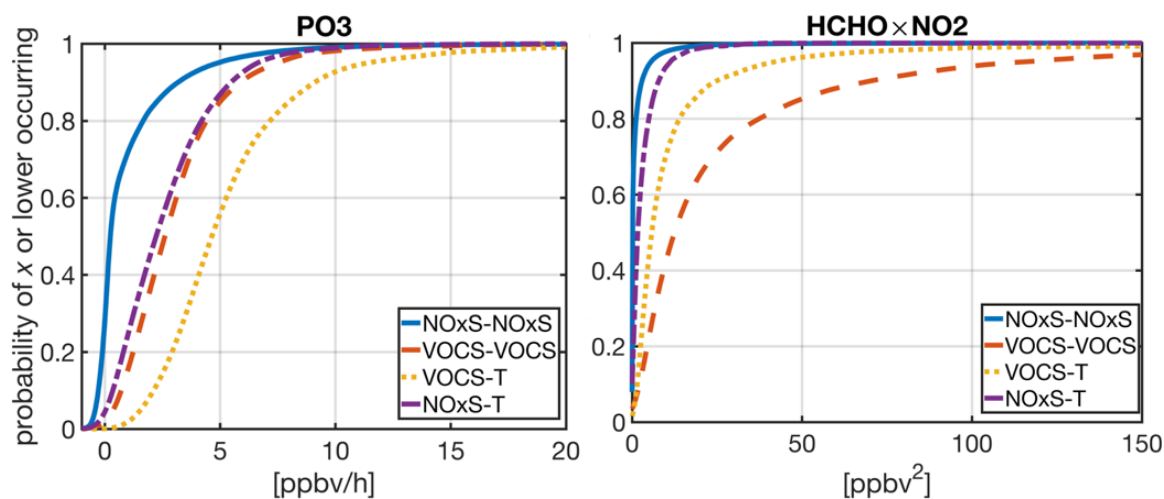
11
1179

1180 **Figure 2.** The comparisons of the observed concentrations of several critical compounds to those
1181 simulated by our FOAM box model. Each subplot contains mean bias (MB), mean absolute bias
1182 (MAB), and root mean square error (RMSE). The least-squares fit to the paired data along with
1183 the coefficient of determination (R^2) is also individually shown for each compound. Note that we
1184 do not account for the observations errors in the x-axis. The concentrations of NO and NO₂ are
1185 log-transformed.



1186
1187
1188
1189
1190
1191
1192
1193
1194
1195

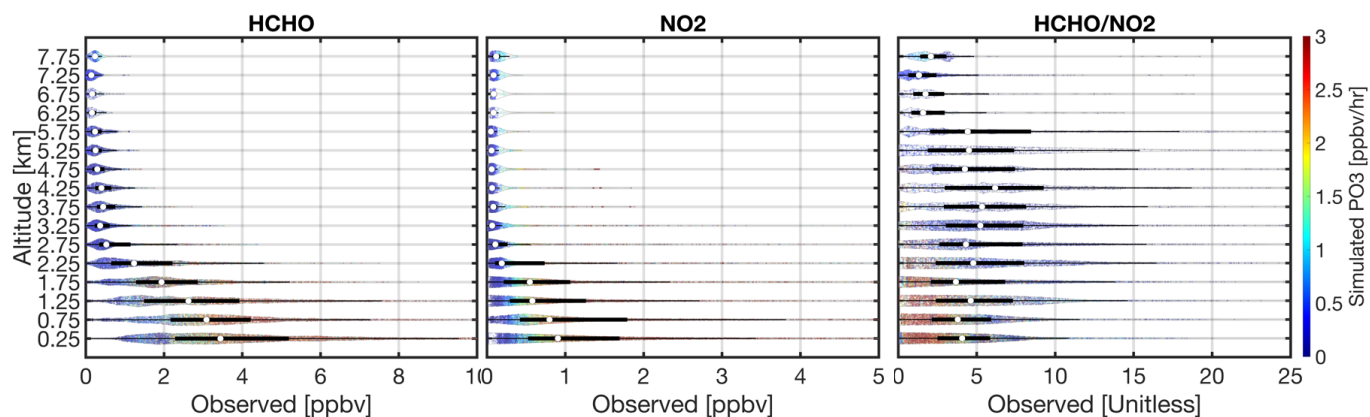
Figure 3. The scatterplot of natural logarithm-transformed of HCHO/NO₂ versus LRO_x/LNO_x based on the simulated values performed by the FOAM box model. The heat color indicates the calculated ozone production rates (PO₃). The size of each data point is proportional to HCHO×NO₂. The light green line is the baseline separator of NO_x-sensitive (above the line) and VOC-sensitive (below the line) regimes. We overlay HCHO/NO₂=1 and HCHO/NO₂=2 as red and purple lines, respectively. The dark green line indicates the least-squares fit to the paired data. The HCHO/NO₂ = 1.8 with 20% error is the optimal transitioning point based on this result.



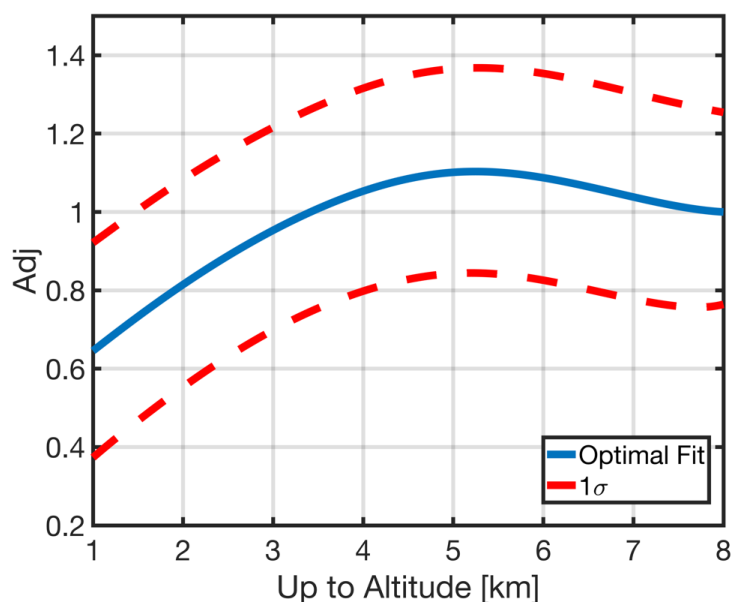
119

1197 **Figure 4.** Cumulative distribution functions of PO_3 and $\text{HCHO} \times \text{NO}_2$ simulated by the box model
1198 constrained by NASA's aircraft observations. Four regions namely as NO_x -sensitive — NO_x -sensitive,
1199 NO_x -sensitive—transitional, VOC-sensitive—transitional, and VOC-sensitive—VOC-sensitive are shown.
1200 The first name of the regime is based on the baseline ($\ln(\text{LRO}_x/\text{LNO}_x)=-1.0$), whereas the second one
1201 follows those defined in Duncan et al. (2010): VOC-sensitive if $\text{HCHO}/\text{NO}_2 < 1$, transitional if
1202 $1 < \text{HCHO}/\text{NO}_2 < 2$, and NO_x -sensitive if $\text{HCHO}/\text{NO}_2 > 2$.

1203

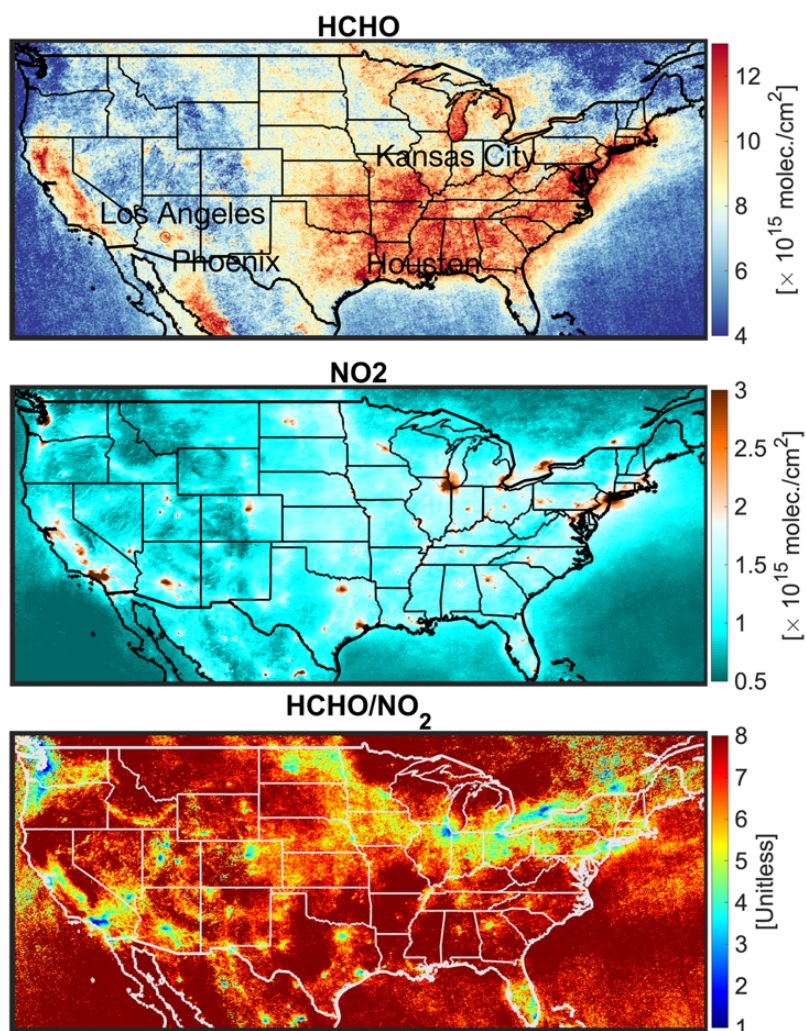


1205 **Figure 5.** The violin plots of the afternoon vertical distribution of HCHO, NO₂, and HCHO/NO₂
1206 observations collected during DISCOVER-AQ Texas, Colorado, Maryland, and KORUS-AQ campaigns.
1207 The violin plots demonstrate the distribution of data (i.e., a wider width means a higher frequency). The
1208 median is shown by white dots. Both 25th and 75th percentiles are shown by a solid black line. The
1209 heatmap denotes the simulated ozone production rates.
1210

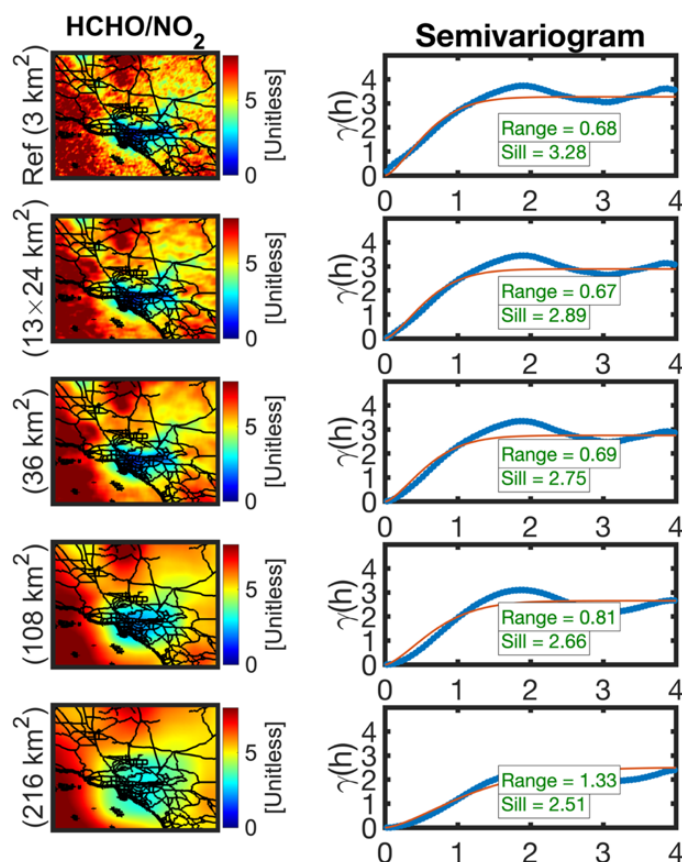


1211
1212
1213
1214
1215
1216
1217
1218
1219

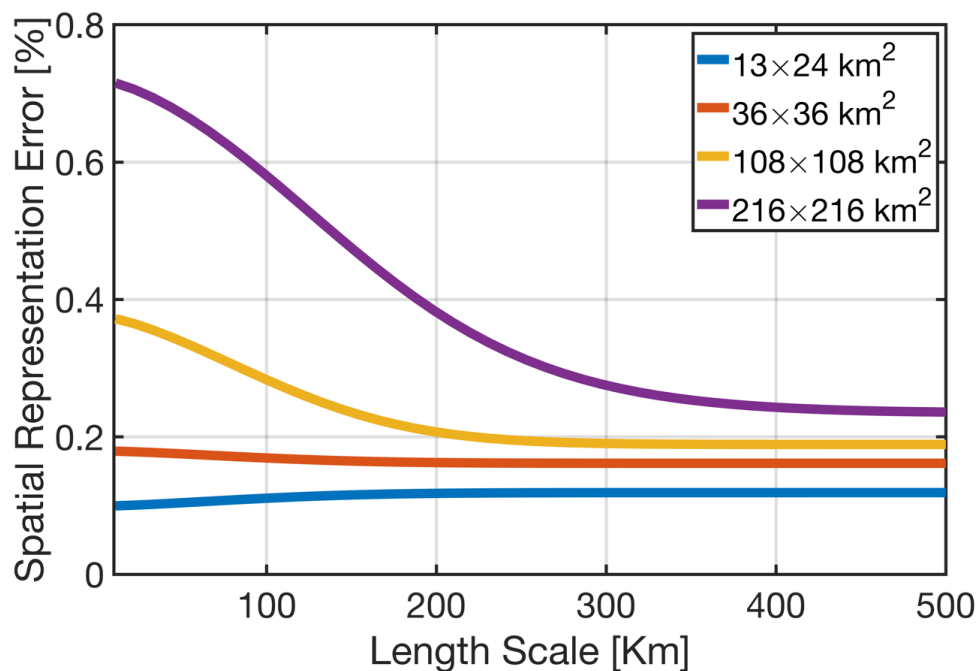
Figure 6. The adjustment factor defined as the ratio of the centroid (first moment) of the polygon bounding 25th and 75th percentiles of the observed HCHO/NO₂ columns by the NASA’s aircraft between the surface to 8 km to the ones between the surface and a desired altitude. This factor can be easily applied to the observed HCHO/NO₂ columns to translate the value to a desired altitude stretching down to the surface (i.e., PBLH). The optimal curve follows a quadratic function formulated in Eq11.



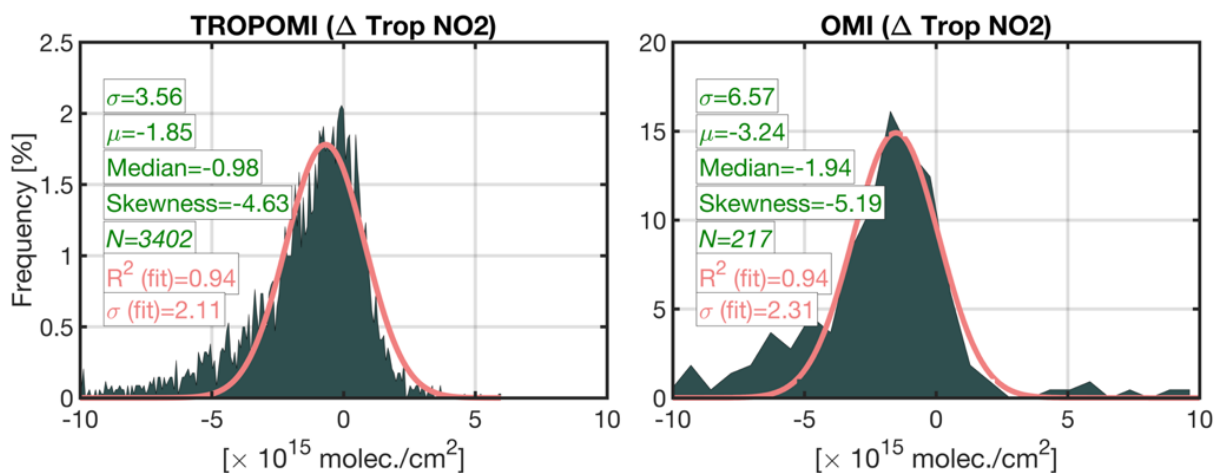
1220
1221 **Figure 7.** Oversampled TROPOMI total HCHO columns (top), tropospheric NO₂ columns
1222 (middle), and the ratio (bottom) at 3×3 km² from June till August 2021 over the US.
1223



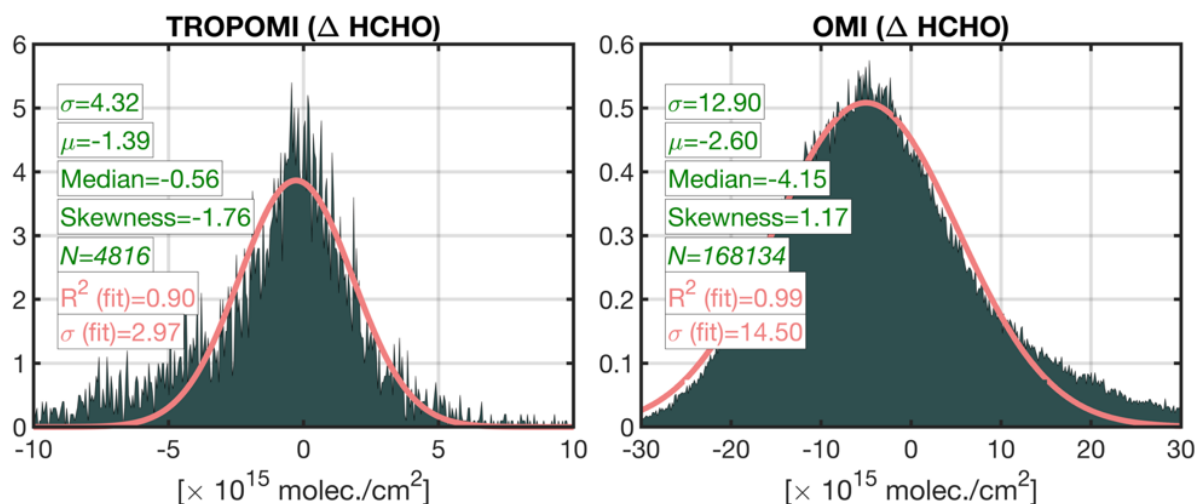
1224
1225 **Figure 8.** The first column represents the spatial map of HCHO/NO₂ ratios over Los Angeles in
1226 June till August 2021 at different spatial resolutions. To upscale each map to a coarser footprint,
1227 we use an ideal box filter tailored to the target resolution. The second column shows the
1228 semivariograms corresponding to the left map along with the fitted curve (red line). The sill and the
1229 range are computed based on the fitted curve. The x-axis in the semivariogram is in degree (1 degree
1230 ~ 110 km).
1231



1232
1233 **Figure 9.** The spatial representation errors quantified based on the proposed method in this study.
1234 The error explains the spatial loss (or variance) due to the footprint of a hypothetical sensor at
1235 different length scales. To put this error in perspective, a grid box with 216x216 km² will naturally
1236 lose 65% of the spatial variance existing in the ratio at the scale of Los Angeles which roughly is
1237 50 km wide. All of these numbers are in reference to the TROPOMI 3x3 km².
1238

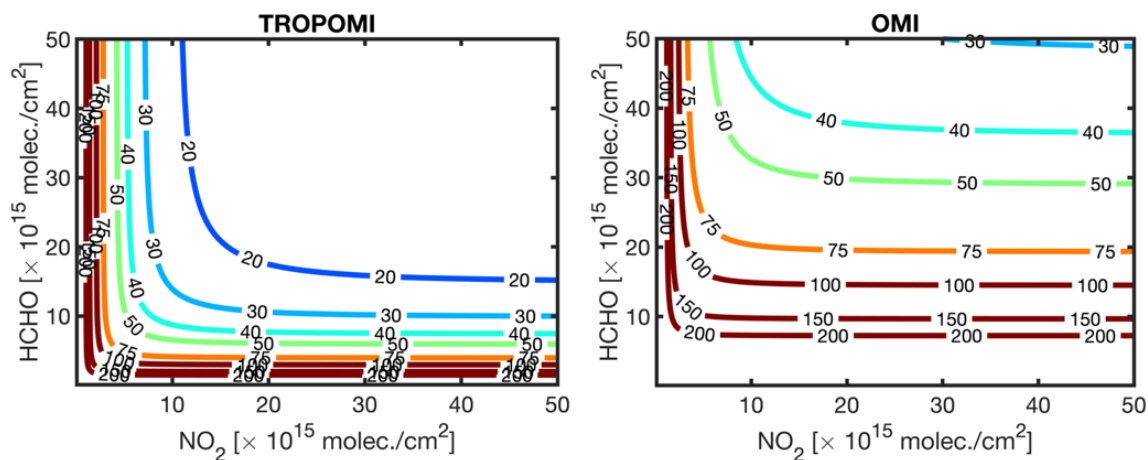


1
1240 **Figure 10.** The histogram of the differences between TROPOMI and OMI and benchmarks. MAX-
1241 DOAS and integrated aircraft spirals are the TROPOMI and the OMI benchmarks, respectively.
1242 The data curation and relevant criteria on how they have been paired can be found in Verholest et
1243 al. (2021) and Choi et al. (2020). The statistics in green color are based on all data, whereas those
1244 in pink are based on the fitted Gaussian function.
1245

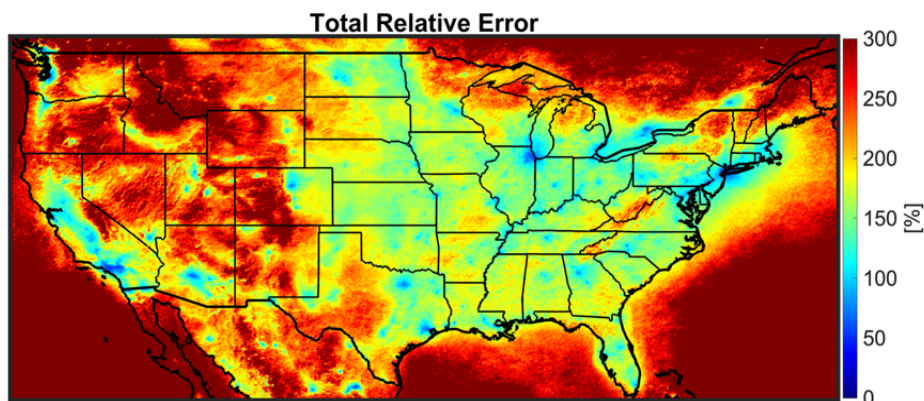


12
1247
1248
1249
1250
1251
1252
1253

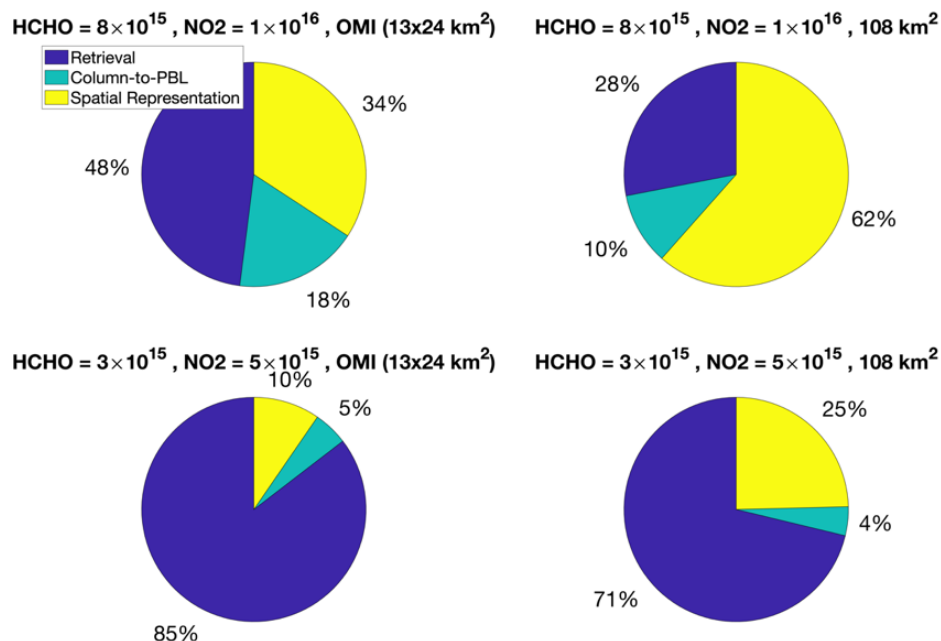
Figure 11. The histogram of the differences between TROPOMI and OMI and benchmarks. FTIR and corrected GEOS-Chem simulations are respectively the TROPOMI and the OMI benchmarks. The data curation and relevant criteria on how they have been paired can be found in Vigouroux et al. (2021) and Zhu et al. (2020). The statistics in green color are based on all data, whereas those in pink are based on the fitted Gaussian function.



1254
1255 **Figure 12.** The contour plots of the relative errors in TROPOMI (left) and OMI (right) based on
1256 dispersions derived from Figure 10 and 11. The errors used for these estimates are based on daily
1257 observations.
1258

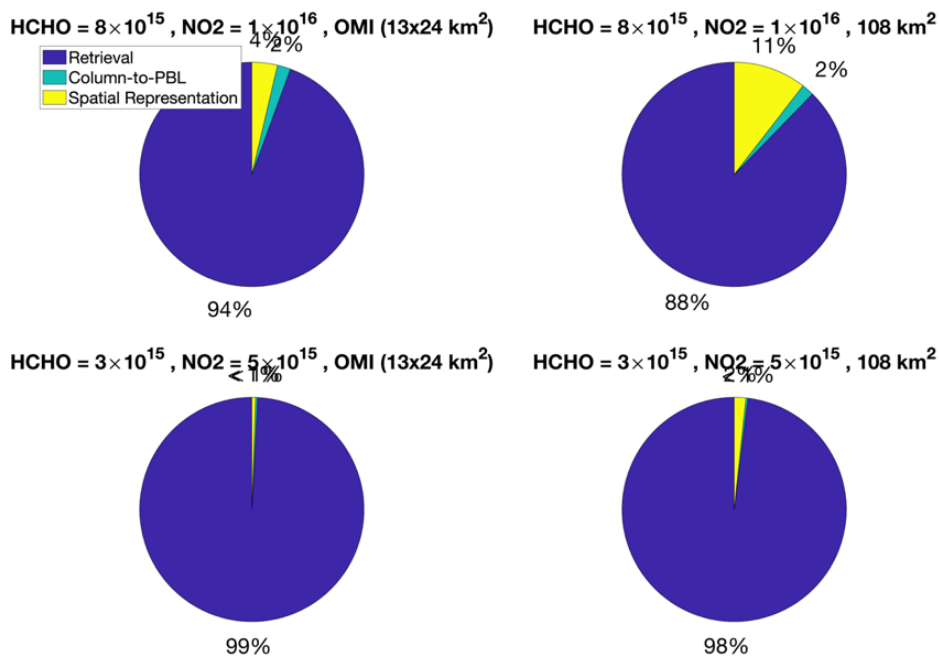


1259
1260 **Figure 13.** The total relative error for observed TROPOMI HCHO/NO₂ ratios considering the
1261 daily TROPOMI retrieval errors ($\sigma_{NO_2} = 2.11 \times 10^{15}$ molec./cm² and $\sigma_{HCHO} = 2.97 \times 10^{15}$
1262 molec./cm²), the spatial representation pertaining to OMI footprint over a city environment (13%
1263 loss in the spatial variance), and the column to the PBL translation parameterization (26%)
1264 proposed in this study. Please note that the observed FNR is based on mean values from June till
1265 August 2021, while the uncertainties used for error calculation are on daily-basis.
1266
1267



1268
1269
1270
1271

Figure 14. The fractional errors of retrieval (blue), column to PBL translation (green), and spatial representation (yellow) of the total error budget for different concentrations and footprints based on TROPOMI sigma values. The retrieval error used for the error budget is on daily basis.



1272
1273
1274

Figure 15. Same as Figure 14 but based on OMI sigma values.